Mélinda Martins

Sedimentological characterization of a sedimentary record from the Portimão Bank (SW Iberia): Late Quaternary-Holocene paleoenvironmental implications.

UNIVERSIDADE DO ALGARVE

FACULDADE DE CIÊNCIAS E TECNOLOGIA

2023

Mélinda Martins

Sedimentological characterization of a sedimentary record from the Portimão Bank (SW Iberia): Late Quaternary-Holocene paleoenvironmental implications.

Master of Science in Marine and Coastal Systems

Work performed under the supervision of:

Profª Dra. Cristina Veiga-Pires (CIMA, UAlg)
Dra. Gemma Ercilla (ICM)
Dra. Teresa Drago (IPMA, IDL)

UAlg
UNIVERSIDADE DO ALGARVE
FACULDADE DE CIÊNCIAS E TECNOLOGIA

2023

Declaração de autoria de trabalho / Declaration of Authorship of work

SEDIMENTOLOGICAL CHARACTERIZATION OF A SEDIMENTARY RECORD FROM THE PORTIMÃO BANK (SW IBERIA): LATE QUATERNARY-HOLOCENE PALEOENVIRONMENTAL IMPLICATIONS

Declaro ser a autora deste trabalho, que é original e inédito. Autores e trabalhos consultados estão devidamente citados no texto e constam da listagem de referências incluída.

I declare to be the author of this work, which is original and unpublished. Authors and works consulted are duly cited in the text and are included in the list of references.

X

Mélinda Martins

Copyright

Acknowledgements

First and foremost, I must thank my supervisors, Profª Dra. Cristina Veiga-Pires, Dra. Gemma Ercilla and Dra. Teresa Drago. I would like to thank you all for your support and valuable advice. Without your dedicated involvement at every stage of my work, this master thesis would never have been realized.

I would also like to thank Prof. Dr. Paulo Fernandes for supporting and guiding me during the analysis of the smear slides. Many thanks to Dra. Filipa Naughton for creating the age model and explaining it to me. And thanks to Dra. Cristina Roque for her amazing assistance and knowledge of trace fossils. I'm very grateful for learning so many things with all of you.

Many thanks to all the researchers who performed data collection, especially the MONTERA research team (from Spain), for offering pre-existing data, and the U-channels of the core on which I based my own study.

I would also like to show my gratitude to Prof. Paulo Relvas, director of our master's program, for always being available to answer any question. To Prof. Luis Nunes and Prof. Joaquim Luis, thank you for your precious help regarding statistical and imagery analysis.

Thank you to my classmates for these two incredible years of master's degree in Portugal, and to the University of Algarve for this wonderful opportunity.

This work has benefited from the infrastructures and equipment's at IPMA Tavira Centre of EDUCOAST, EEAGrants - Nature-Based Education in Coastal Geosciences – A field station in southern Portugal (PT-INNOVATION-067), and EMSO-PT- European Multidisciplinary Seafloor and water column Observatory (Pinfra/22157/2016) projects.

I would also like to thank my colleagues from the IPMA Tavira for these great moments spent together at the station. Thank you for your support and your welcome.

Many thanks to my friends Gustavo Marino, and Jacqueline Santos, for reading, correcting my English, and making great suggestions for this master thesis.

Finally, I must express my very profound gratitude to my parents, and to my partner, for providing me with unfailing support and continuous encouragement throughout my years of study, and through the process of working and writing this master thesis.

Abstract

Over the centuries, Earth's oceans have served as repositories of invaluable historical data within their sedimentary layers. Deep-sea sedimentary archives collected through sedimentary cores constitute essential reservoirs of complete information for the reconstruction of paleoenvironments. The present study focuses on the re-examination of a sedimentary core, piston core named PC06, extracted at the base of the Portimão bank, located southwest of the Iberian margin. This core spans the last 49,000 years of Earth's history and was collected at a depth of 3 520 meters of water as part of the Spanish MONTERA project, entitled “Seamounts of the Southern Iberian Peninsula: tectonics and sedimentation” (CTM 2009-14157-C02 CSIC). The main objective of this work was to identify and characterize the paleoenvironmental conditions prevailing during this period, through a multidisciplinary study, including sedimentological, mineralogical, and geochemical analyses. Our analysis reveals environmental changes close to Portimão Bank during the Late Pleistocene and Holocene. Four lithofacies define distinct sedimentary units, reflecting conditions dating from 49,000 years BP to the present. Notable periods, including the Last Glacial Maximum and the Holocene, highlight the impact of climate, sea level changes, and ocean circulation and productivity on sediment characteristics. The study emphasizes the role of bottom currents and their potential link to deep water flow in the North Atlantic, and the presence of pyrite throughout the sedimentary record indicates the impact of anoxic conditions, influencing the transition from an anoxic environment to a well-oxygenated environment. Furthermore, the study highlights the complexity of deep-water transport, highlighting the influence of the Portimão Bank on sedimentation patterns. Overall, the analysis provides a nuanced understanding of the environmental evolution of the Portimão Bank over the past 49,000 years. These findings have broader implications for our understanding of past climatic and oceanographic conditions and their impact on sedimentation processes in this region.

Keywords: Sedimentary archives; Paleoenvironments; Portimão Bank; Gulf of Cadiz; Sea level; Bottom currents; Ocean productivity; Anoxic; Climatic conditions; Oceanographic conditions; Sedimentation processes.

Resumo Alargado

O estudo dos sedimentos marinhos de grandes profundidades é fundamental para compreender o clima da Terra e os oceanos, uma vez que esses sedimentos contêm uma riqueza de dados relativos ao passado. Através da análise detalhada de amostras provenientes desses sedimentos, é possível reconstruir condições ambientais passadas, desvendando flutuações de temperatura, das correntes oceânicas e do nível do mar. A pesquisa paleoambiental constitui uma base sólida para nossos esforços em direção à preservação do futuro do planeta e ao fortalecimento da nossa resiliência diante dos desafios ambientais. Nesse contexto, o Golfo de Cadiz, localizado na confluência do Oceano Atlântico e do Mar Mediterrâneo, emergiu como uma região crucial para estudos paleoambientais, devido à sua singular dinâmica geológica e oceanográfica. O Monte de Portimão, um proeminente monte submarino situado na parte oeste do Golfo de Cadiz, exerce uma influência significativa nos processos sedimentares e oceanográficos dessa região.

Várias iniciativas de pesquisa, incluindo o projeto espanhol MONTERA "Montes submarinos da Península Ibérica meridional: tectônica e sedimentação" (CTM 2009-14157-C02 CSIC), focaram seus esforços nessa região e resultaram na colheita de diversas amostras de sedimentos. Uma dessas amostras, a sondagem PC06, recuperada da base do Monte de Portimão a uma profundidade de 3.520 metros, é o foco central de nossa investigação. Os nossos principais objetivos envolvem uma análise multidisciplinar dessa sondagem, abrangendo os últimos 49.000 anos, com uma dupla ênfase: primeiro, decifrar as principais transformações paleoambientais registadas na sondagem e, segundo, desvendar a origem e natureza das lentículas pretas intercaladas ao longo do sedimento da sondagem. Através da aplicação de uma abordagem multidisciplinar, incluindo análises sedimentológicas, mineralógicas e geoquímicas, almejamos identificar as fontes dessas lentículas, elucidar os processos de deposição associados e avaliar as suas implicações paleoambientais durante um período relativamente pouco estudado.

A nossa investigação da sondagem PC06 oferece perceções profundas sobre a complexa interação entre as flutuações do nível do mar, as correntes de fundo e a produtividade primária, que moldaram as sequências sedimentares no Golfo de Cadiz. A interpretação sedimentar-estratigráfica da sondagem PC06 fornece informações valiosas sobre as mudanças ambientais que ocorreram durante os períodos do Pleistoceno Tardio e Holoceno. Quatro principais litofácies (lama pirática, lama rica em matéria orgânica e pirita, lama rica em argila e lama pelágica) definem unidades sedimentares, cada uma refletindo condições e processos específicos. Períodos notáveis, como o Último Máximo Glacial e o Holoceno, destacam o impacto de condições climáticas, mudanças no nível do mar e circulação e produtividade oceânica nas características sedimentares.

O registo sedimentar apresenta uma transição da predominância de sedimentos terrígenos durante o período glacial para a predominância de sedimentos (hemi)pelágicos no Holoceno. Essas mudanças são atribuídas à interação das oscilações do nível do mar, correntes de fundo e variações na produtividade oceânica. Durante o último período glacial, caracterizado por níveis do mar mais baixos, ocorreu um substancial influxo de sedimentos terrígenos de regiões costeiras expostas.

A transição de lamas ricas em pirita e matéria orgânica para lamas ricas em argila durante o último máximo glacial representa uma mudança de condições anóxicas para condições bem oxigenadas, influenciada por alterações nos padrões oceanográficos. Picos distintos de silte e valores elevados da mediana granulométrica (D50) durante eventos climáticos específicos, como o ‘Younger Dryas’, destacam a profunda influência das correntes de fundo no transporte de sedimentos ao redor do Monte de Portimão. Essas correntes também impactam na erosão de características topográficas, incluindo o Monte de Portimão, e facilitam a formação de contourites.

É interessante de notar que a abundância de coccolitoforídeos nas amostras sedimentares de PC06 durante o Holoceno aponta para uma maior produtividade oceânica, provavelmente impulsionada por temperaturas oceânicas mais quentes e maior insolação. A presença de pirita ao longo da sondagem indica o impacto de condições anóxicas, influenciando a transição de ambientes anóxicos para bem oxigenados.

No entanto, é fundamental reconhecer as limitações deste estudo. Muitas questões persistem, enfatizando a necessidade de pesquisas adicionais para aprofundar a nossa compreensão dos processos sedimentares no Golfo de Cadiz, especialmente em regiões como o Monte de Portimão.

Palavras-chave: Arquivos sedimentares; Paleoambientes; Monte de Portimão; Golfo de Cadiz; Nível do mar; Correntes de fundo; Produtividade oceânica; Anóxico; Condições climáticas; Condições oceanográficas; Processos de sedimentação.

Table of Contents

List of Figures

List of Tables

List of Abbreviations

AC	Azores Current
AMOC	Atlantic Meridional Overturning Circulation
BI	Bioturbation index
BP	Before Present
BSF	Below seafloor
$CaCO_3$	Calcium carbonates
CCD	Carbonate Compensation Depth
D-O	Dansgaard-Oeschger events
ENACW	Eastern North Atlantic Central Water
GS	Gulf Stream
HE	Heinrich event
LGM	Last Glacial Maximum
LOI	Loss on Ignition
MIS	Marine Isotope Stage
MONTERA	Seamounts of the southern Iberian: tectonic and sedimentation
MOW	Mediterranean Outflow Water
MSCL	Multisensor core logger
MSL	Mean sea level
NADW	North Atlantic Deep Water
OM	Organic matter
OMZ	Oxygen Minimum Zone
PB	Portimão Bank
PCA	Principal Component Analysis
PP	Primary Productivity
SPM	Suspended Particulate Matter
SST	Sea Surface Temperature
XR	X-ray radiography
XRF	X-ray fluorescence
YD	Younger Dryas

1 INTRODUCTION

The world's oceans have, for centuries, hidden a wealth of historical data in the layers of sediment that cover the ocean floor. As humanity faces pressing contemporary environmental issues, our quest for a deeper understanding of Earth's complex past becomes increasingly imperative. In this context, the Gulf of Cadiz, a dynamic region nestled in the northeast Atlantic Ocean where the Atlantic Ocean and the Mediterranean Sea converge, emerges as a hub for paleoenvironmental research (i.e., Terrinha et al. 2009; Salgueiro et al. 2014; Vazquez et al. 2015; Roque et al. 2016; Silva et al. 2020; Vandorpe et al. 2022; Murray-Wallace 2023).

The Gulf of Cadiz, located in the southwestern part of the Iberian Peninsula, is a region of remarkable geological and oceanographic dynamism (i.e., Villanueva and Gutierrez-Mas 1994; Terrinha et al. 2009; Wienberg et al. 2010; Roque et al. 2016; Silva et al. 2020). Its sedimentary processes are intricately controlled by a combination of factors (see Chapter 4), making it a fascinating area of study for geologists, oceanographers, and researchers interested in the Earth's history. A significant portion of scientific research focuses on sediment cores extracted from this region (i.e., Colmenero-Hidalgo et al. 2004; Ferreira et al. 2008; Terrinha et al. 2009; Gràcia et al. 2010; Mestdagh et al. 2019; García et al. 2020; Silva et al. 2020; Murray-Wallace 2023) telling the story of environmental transformations spanning millennia.

Through careful analysis of these sediment cores, we can reconstruct past environmental conditions, deciphering temperature fluctuations, ocean currents, and sea levels. Additionally, these records give us insight into the complex interconnections between climate, oceanography and the ecosystems that have thrived in the Gulf of Cadiz throughout geological eras (i.e., Rodrigo-Gámiz et al. 2011; García et al. 2020; Meinander et al. 2022; Penaud et al. 2022; Murray-Wallace 2023).

Therefore, it has been the subject of numerous research efforts, like those carried out by the researchers cited above, and in particular the Spanish MONTERA project “Seamounts of the southern Iberian Peninsula: tectonics and sedimentation” (CTM 2009-14157-C02 CSIC). As part of this project, several sediment cores were collected in the Gulf of Cadiz. One of these cores, deep-sea piston core PC06, is the focus of the present study, allowing to reconstruct paleoenvironmental conditions near the Portimão Bank over the past 49,000 years. Through a detailed examination of the PC06 core, collected at 3520 m water depth, in the abyssal plain, we aim to contribute to a broader understanding of paleoenvironmental dynamics.

To carry out a complete paleoenvironmental study, it is essential to consider a set of parameters acting at these depths. These parameters encompass not only the sedimentation processes that have shaped the geologic record, but also the complex interplay of climate variability, paleoceanographic conditions, and unique local features specific to the study area (i.e., Terrinha et al. 2009; Gràcia et al. 2010; Mestdagh et al. 2019; García et al. 2020; Silva et al. 2020; Murray-Wallace 2023).

Sedimentation processes lay the foundation for interpreting historical records embedded in sedimentary layers, providing insight into past events (i.e., Terrinha et al. 2009; Silva et al. 2020). Climate variability data allows us to discern long-term climate trends, shedding light on Earth's response to environmental change (i.e., Voelker et al. 2007; Stumpf et al. 2011; Meinander et al. 2022). Paleoceanographic conditions, such as ocean circulation patterns and sea surface temperatures, further enrich our understanding of how the oceans influenced and were influenced by the surrounding environment (i.e., Salgueiro et al. 2014; García et al. 2020; Martorelli et al. 2021). Finally, local geological and oceanographic features, ranging from topography to currents, provide critical context because they shape the specific conditions under which paleoenvironmental reconstructions take place. Our approach integrates these various parameters which are fundamental to reconstruct the environmental history of our study area.

1.1 Deep-sea sedimentation

Modern sediment distribution in the ocean is determined by the sediment sources, as well as the physical and chemical factors that control deposition. Most terrigenous sediments are deposited on continental margins along the shore, including river deltas, bays, estuaries, and continental margins. Pelagic sediment, on the other hand, is restricted to the bathyal depths (i.e., Nichols 2009; Hesse and Schacht 2011; Hüneke and Henrich 2011; Rajput and Thakur 2016; Cochran et al. 2019).

Deep-sea sediments represent the most widespread and complete record of past oceanic and climatic states. The composition and distribution of deep-sea sediments is the result of a multitude of climatic, biotic, and oceanic conditions relating to biogeochemical cycles and environmental changes (i.e., Hesse and Schacht 2011; Rajput and Thakur 2016; Wade et al. 2020). Therefore, the study of paleo-sediment records facilitates the examination of oceanic and climatic changes including but not limited to ocean productivity, carbonate chemistry, and glacial processes (i.e., Shepard 1977; Hesse and Schacht 2011; Wade et al. 2020).

Deep-sea sediments are the product of three major processes: gravity-driven downslope deposition (density current), along slope bottom current activity, and slow pelagic settling (see Figure 1) through the water column (i.e., Hüneke and Henrich 2011; Hesse and Schacht 2011; Lagabrielle et al. 2013; Rajput and Thakur 2016).

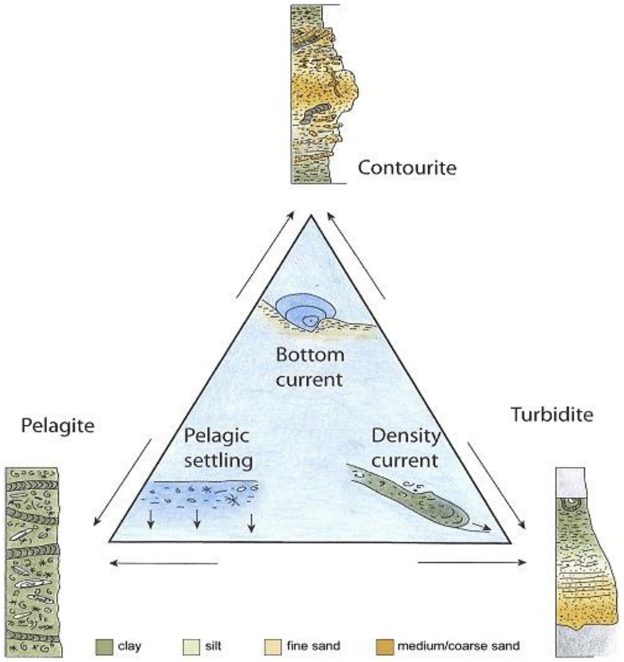

Figure 1. Conceptual diagram showing the three major processes operating in the deep sea (within the triangle) and the facies model of the respective depositional products (extracted from Rogerson et al. 2014).

1.1.1 *Gravity-driven sediment transport*

Most sediments coming from the continent are transported to the deep sea via a variety of gravity-driven forms of movement, including sliding, slumping, and sediment-gravity flows (i.e., Nichols 2009; Lagabrielle et al. 2013; Rajput and Thakur 2016; Cochran et al. 2019) as it is illustrated in Figure 2.

Slides, slumps, debris flows, and turbidity currents are caused by gravity-induced slope instability and are geological processes that affect the submarine terrain. They can transport sediment over great distances and generate distinctive sedimentary features on the seafloor, such as submarine canyons, deep-sea fans, and sediment deposits (see Figure 1) (i.e., Nichols 2009; Gràcia et al. 2010; Lagabrielle et al. 2013; Cochran et al. 2019).

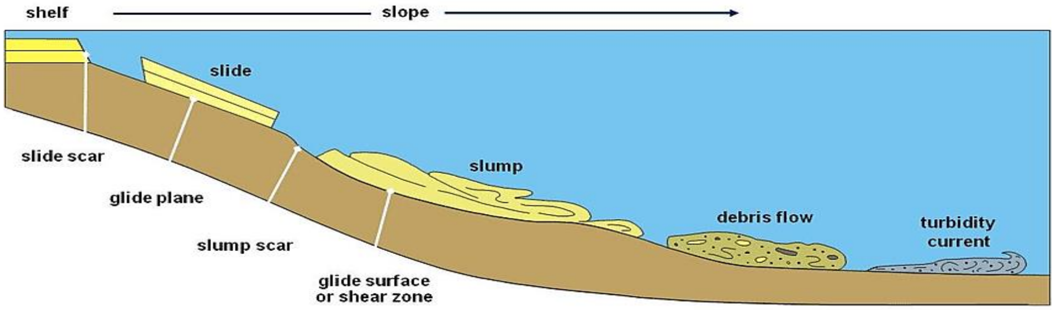

Figure 2. Schematic diagram illustrating the gravity-driven transport processes - slide, slump debris flow and turbidity current (modified from Bal and Gaafar 2014).

A turbidity current is a form of gravitational current driven by excess density due to suspended sediment in flows (i.e., Cochran et al. 2019). Turbulence keeps most of the sediment in suspension and carries new material out of the bed, as some of the sediment is deposited. Turbidity currents generally have low sediment concentrations, with a volume concentration $\leq 23\%$ (i.e., Shepard 1977; Nichols 2009; Lagabrielle et al. 2013; Cochran et al. 2019).

In nature, turbidity currents are primarily initiated by sediment erosion or partial transformation of impulsively triggered submarine slides, slump, or debris flows, as illustrated in Figure 2. In a geomorphological context, a turbidity current is a type of sediment mass movement on continental margins, responsible for the transport of encrusted sediments from shallow waters and their deposition in the ocean depths (i.e., Nichols 2009; Lagabrielle et al. 2013; Cochran et al. 2019).

1.1.2 *Bottom currents*

It is increasingly recognized that bottom currents are important transport and sedimentary phenomena that control much of the sedimentation of deep waters (i.e., Shepard 1977; Rebesco et al. 2014). Along-slope bottom currents are ocean flows parallel to seafloor contours, which closely follow underwater topography, such as coastlines, continental shelves, or canyons and seamounts. These currents are influenced by a combination of factors, including wind, temperature, and salinity gradients, and they can play an important role in shaping coastal and deep-water environments (i.e., Shepard 1977; Marchès et al. 2007; Rebesco et al. 2014).

In fact, bottom currents along slopes have diverse impacts, from the transport of sediment and nutrients that nourish marine ecosystems to the stability of coastal structures. To simplify, any "persistent" water current near the seabed can be considered a bottom current (i.e., Shepard 1977; Rebesco et al. 2014).

The sediments deposited by bottom currents are named contourites (see Figure 1) (i.e., Llave et al. 2006; Marchès et al. 2007; Rebesco et al. 2014). The extensive distribution of contourites is linked to the pervasiveness of the transport currents that influence their deposition: bottom currents and other oceanographic phenomena (see Figure 3) (i.e., Llave et al. 2006; Marchès et al. 2007; Rebesco et al. 2014; Cochran et al. 2019; García et al. 2020; Martorelli et al. 2021).

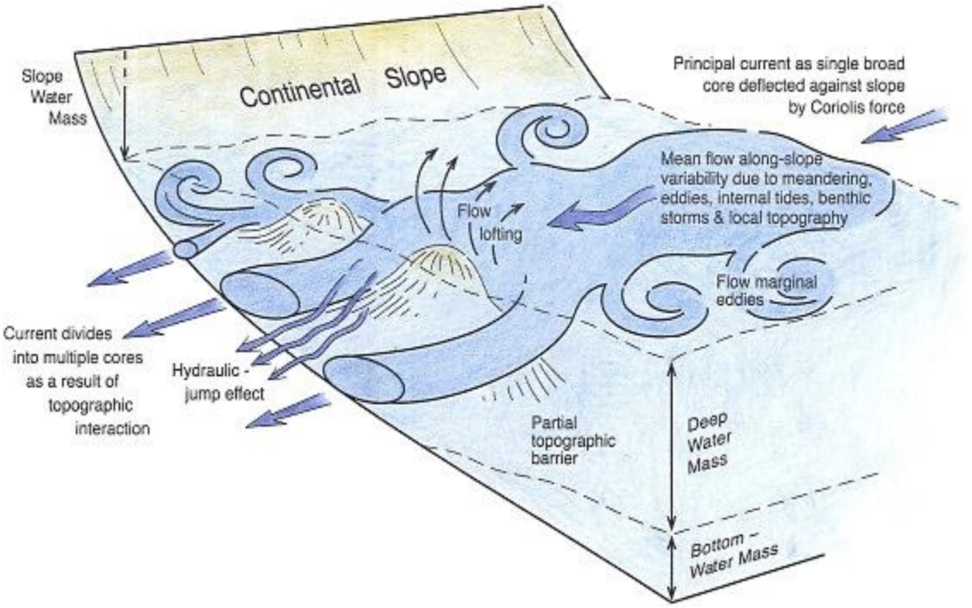

Figure 3. Schematic diagram summarising the principal bottom-current features (extracted from Rogerson et al. 2004).

1.1.3 Settling of pelagic particles

Pelagic sedimentation (see Figure 1) happens at various scales in the open ocean and become dominant only in very remote abyssal areas. As a background signal, the daily process is a gradual and continuous rain of biogenic debris produced mostly by planktic flora and fauna in the upper water column, as explained by Hüneke and Henrich (2011).

Furthermore, distinct regions of the ocean exhibit pronounced, short-term, often seasonal sedimentation pulses following biogenic bloom events, such as the yearly coccolith blooms, which begin at low latitudes in late spring to early summer and spread to higher latitudes in summer and early autumn (i.e., Hüneke and Henrich 2011). As Hüneke and Henrich (2011) pointed out, a considerable amount of this material, which consists of calcareous and siliceous skeletal remains as well as soft organic tissue, falls to the sea floor as marine snow and faecal pellets due to gravity.

The distribution of pelagic sediments is linked to a dynamic balance in marine environments. In warmer, shallower waters, carbonate particles, primarily consisting of calcium carbonate (CaCO3), are dominant due to increased biological productivity and the prevalence of calcium-secreting organisms such as foraminifera and coccolithophores (i.e., Colmenero-Hidalgo et al. 2004; Hillaire-Marcel and De Vernal 2007; Cochran et al. 2019). Conversely, in colder, nutrient-rich waters, siliceous particles, mainly composed of silica (SiO2), predominate, and thrive in habitat suitable for diatoms and radiolarians (i.e., Hillaire-Marcel and De Vernal 2007; Hüneke and Henrich 2011). This complex distribution pattern results from multifaceted interactions between temperature regimes, nutrient availability, and metabolic trends of marine organisms. Collectively, these factors contribute to the nuanced and complex patterns of carbonate and siliceous pelagic particle deposition, shaping the seafloor of oceans (i.e., Hillaire-Marcel and De Vernal 2007; Hüneke and Henrich 2011; Cochran et al. 2019).

1.2 Accumulation and preservation of deep-sea sediments

Deep-sea sediments represent the most widespread and complete record of Cenozoic oceanic and climatic state. The pattern and composition of seafloor sediments seaward of the continental shelf reflects biological, geochemical, terrestrial, and climatic conditions on Earth at the time of deposition (i.e., Hesse and Schacht 2011; Chester and Jickells 2012; Wade et al. 2020).

The accumulation of deep-sea sediments requires two fundamental requirements: (1) sedimentation of materials and (2) low-oxygen conditions (i.e., Hesse and Schacht 2011; Hüneke and Henrich 2011; Magill et al. 2018; Wade et al. 2020).

Deep sea sediments form due to the gradual accumulation of various materials over time. These materials can include mineral particles, organic matter (OM), microorganisms, and even remains of marine organisms such as plankton, shells, and corals. The accumulation of these materials can be influenced by factors such as water currents, sedimentation rates, oxygen content and the availability of sediment sources. This is the case for biogenic pelagic sediments, which are fed by dying surface plankton whose tests or shells, either calcium carbonate or siliceous, sink along the water column (i.e., Hüneke and Henrich 2011; Wade et al. 2020).

Deep-sea sediments typically thrive in environments with low oxygen content, a condition known as "hypoxia" or "anoxia." This low-oxygen environment is crucial for preserving OM and preventing its rapid degradation. In the absence of oxygen, OM can accumulate and undergo anaerobic decomposition, leading to the formation of substances like methane and carbon dioxide (i.e., Hesse and Schacht 2011; Chester and Jickells 2012; Magill et al. 2018; Wade et al. 2020). For hemipelagic sediments, the oxidation of OM is the driving force behind diagenetic reactions. In the absence of oxygen in the deep sea, OM undergoes anaerobic decomposition and is primarily degraded by a diverse community of microorganisms, primarily bacteria. Oxidation of OM in deep-sea sediments is a critical biogeochemical process that plays a key role in marine ecosystems and the global carbon cycle (i.e., Hesse and Schacht 2011; Chester and Jickells 2012; Magill et al. 2018; Wade et al. 2020).

Sediments preservation typically depends on environmental and sedimentological conditions, such as a sufficiently high sedimentation rate, and severe depletion of dissolved oxygen in bottom water to inhibit bioturbation by macrobenthos (i.e., Hesse and Schacht 2011; Wade et al. 2020).

Additional oceanographic factors include the strength and depth range of the Oxygen Minimum Zone (OMZ), the Carbonate Compensation Depth (CCD), and regional anthropogenic eutrophication from point sources such as large, polluted rivers (i.e., Burton 1998; Paulmier and Ruiz-Pino 2009; Lagabrielle et al. 2013). The OMZ is the region of the ocean (subsurface oceanic zones) where seawater oxygen saturation is lowest. Depending on the local environment, including biological, chemical, and physical processes, this zone can be found at water depths between 50 and 200 m (i.e., Paulmier and Ruiz-Pino 2009). CCD is the specific depth of the ocean where calcium carbonate minerals dissolve in the water more quickly than they can accumulate. Dissolution occurs more quickly below the CCD, so that carbonate particles dissolve and the carbonate shells of organisms are not preserved (i.e., Burton 1998; Lagabrielle et al. 2013).

1.3 Climate variability over the last 50,000 years

The environmental conditions of the oceans are strongly linked to climatic variations. Climate forcing in the oceans refers to the external or determinant factors that influence and impact the temperatures, oceanic circulation, and general behaviour of the ocean at different time scales (i.e., Waelbroeck et al. 2001; Salgueiro et al. 2014; Vandorpe et al. 2022).

The Quaternary is characterized by a succession of glacial and interglacial periods and by consequent eustatic changes, modulated by Milankovitch cycles. These variations in precession, obliquity and eccentricity control solar radiation, climate cycles and sea level variations through changes in the volumes of the global ice sheet (i.e., Roque al. 2010; Mestdagh et al. 2019; Murray-Wallace 2023). In fact, major changes have been repeatedly observed through glacio-eustatic sea level changes, resulting from fluctuating ice volumes in response to changes in insolation recorded at the Earth's surface. When temperatures drop, huge ice sheets develop and cover a significant portion of the Earth's surface. On the other hand, when temperatures rise, ice caps melt, and sea levels rise. These cycles saw the slow, gradual buildup of continental-scale ice sheets and an average fall in sea level of -130 to -120 m over a period of almost 100,000 years. The last ice age ended approximately 10,000 years ago (i.e., Scott-Elias 2007; Genty and Moreno 2021; Murray-Wallace 2023).

Glacial and interglacial periods are associated with the Milankovitch cycles, and are phases dividing the Quaternary period, defined by the actual record of oxygen isotope temperature. As determined by oxygen isotope measurements, each Quaternary climate phase has a marine isotope stage (MIS) number that identifies alternately warmer and colder temperature periods (i.e., Scott-Elias 2007; Genty and Moreno 2021; Murray-Wallace 2023).

The Late Quaternary period, marked by significant climatic fluctuations accompanied by rapid environmental changes, begins after the last major ice age, known as the Pleistocene epoch. The transition from the Pleistocene to the Holocene is marked by the last major abrupt climate change event known as the Younger Dryas (YD). YD is a cool period between about 12,900 and 11,600 years ago that disrupted the dominant warming trend that was occurring in the Northern Hemisphere during the late Pleistocene. The YD was characterized by cooler average temperatures that returned parts of Europe and North America to Ice Age conditions. After this period ended, a period of rapid warming followed, and average temperatures increased to near current levels. The YD event (see Table 1) marks the transition between two steps of deglacial warming characterised by pulses of meltwater inputs (i.e., Scott-Elias 2007; Roque et al. 2010; Genty and Moreno 2021; Murray-Wallace 2023).

Past glacial periods were also punctuated by abrupt pseudo-periodic oscillations in temperature (described as Dansgaard-Oeschger cycles, or stadials-interstadials, and Heinrich events), particularly well-marked in paleorecords from mid- and high latitudes of the Northern Hemisphere (Greenland ice cores, ocean and lake sediments, and cave stalagmites).

The Dansgaard-Oeschger cycles (D-O) typically began with a sudden warming of Greenland of 10 to 15°C over several decades and persisted for about 500 to more than 2,000 years (i.e., Dansgaard et al. 1993). So far, 25 events have been identified with an apparent periodicity of 1,600 years. D-O cycles, which took place during the last glacial period (115,000 – 11,700 years ago). According to Genty and Moreno (2021), these events are distinguished by abrupt temperature fluctuations, with relatively warm interstadials followed by rapid cooling into stadials (i.e., Scott-Elias 2007; Genty and Moreno 2021; Murray-Wallace 2023).

Table 1. Summary of several events that occurred over the last 50 kyrs *Before Present (BP). The information is extracted from the International Chronological Chart of the International Commission on Stratigraphy (ICS) and Genty and Moreno (2021).

ICS stages		Event dates (kyrs BP)	Event names
QUATRENARY	Holocene	8,2	Holocene cold event
	Late Pleistocene	11,7-12,9	Younger Dryas (YD)
		~ 16.8	Heinrich event 1 (HE1)
		18-23	Last Glacial Maximum (LGM)
		~ 24	Heinrich event 2 (HE2)
		~ 31	Heinrich event 3 (HE3)
		~ 38	Heinrich event 4 (HE4)
		~ 45	Heinrich event 5 (HE5)

Furthermore, large iceberg discharges known as Heinrich events (HE) (see Table 1) occurred between 40° and 55° N, carrying coarse-grained particles debris, known as ice-rafted debris or IRD, into the North Atlantic Ocean (i.e., Genty and Moreno 2021). The melting icebergs released their basal sediments, depositing them on the ocean floor. More than half a dozen HE occurred during the last ice age, approximately every 10,000 years, 135,000 to 12,000 years ago. HE adds large amounts of fresh water to the ocean, impacting global climate, but most strongly in the Northern Hemisphere.

The Last Glacial Maximum (LGM) (see Table 1) was a period in the last ice age when the climate on Earth was the coldest and the size of the ice sheets was at their largest. The Last Glacial Maximum occurred approximately 20,000 years ago, during the Pleistocene epoch. The timing of the LGM coincides with a strong summer insolation minimum in mid-to-high northern latitudes due to orbital cycles, and thus is naturally explained by Milankovitch's glaciation theory. Between the LGM and the beginning of the Holocene, approximately 11,650 years ago peak summer insolation in the north increased by approximately 40 to 50 W/m^2 (i.e., Genty and Moreno 2021). This massive increase in solar heating was responsible for the deglaciation of the Northern Hemisphere and the resulting rise in mean sea level of around 130 m. (i.e., Scott-Elias 2007; Genty and Moreno 2021; Murray-Wallace 2023).

1.3.1 Paleoclimatic conditions in SW Iberian continental margin

The melting of icebergs and subpolar waters reached the Iberian margin during the Heinrich events (HE) and Younger Dryas (YD) episodes (i.e., Rodrigo-Gámiz et al. 2011; Murray-Wallace 2023). Therefore, several records served to demonstrate the connection between oceanographic and atmospheric oscillations during the last glacial cycle, supporting a strong link between the Mediterranean and North Atlantic climates (i.e., Rodrigo-Gámiz et al. 2011; Nichols et al. 2020; Vandorpe et al. 2022).

Colder periods of the last glacial period, including Heinrich events (HE) (see Table 1), and Dansgaard-Oeschger (D-O) events, are characterised by increased aeolian dust supply and stronger bottom currents (i.e., Itambi et al. 2009; Stumpf et al. 2011; Meinander et al. 2022; Vandorpe et al. 2022). Moreover, these periods present higher input of terrigenous (aeolian origin) material, and an increase in primary productivity (PP) (i.e., Penaud et al. 2022). Additionally, Llave et al. (2006) demonstrated that higher sedimentation rates occur during periods of ice melt or cold to warm transitions.

Salgueiro et al. (2014) explained that the hydrography and associated productivity of the Iberian margin have undergone significant changes in the past. Indeed, ocean PP helps to explain past and present biogeochemical cycles and climate changes in the oceans (i.e., Penaud et al. 2022). The Gulf of Cadiz is not presently a carbon sink area, but its state was different under glacial regimes. Nevertheless, the area was characterised by high PP during the last glacial period. High PP may be related to nutrient replenishments in surface waters by runoff as Penaud et al. (2022) revealed. PP periods are linked to the dynamics of upwelling, active almost year-around during stadial (cold periods) but restricted to spring-summer during interstadials like today. Intensified and/or longer seasonal functioning of upwelling allowed the maintenance of sustained PP levels, combined with lower remineralization of OM contributing to carbon sequestration (i.e., Brüchert et al. 2000; Hüneke and Henrich 2011; Penaud et al. 2022).

Additionally, PP can also be influenced by dust fluxes. Indeed, significant flows of dust towards the ocean act as a fertilizer for PP (i.e., Itambi et al. 2009; Penaud et al. 2022). In general, high dust fluxes are recorded during the glacial period and low dust fluxes during the interglacial period as Voelker et al. (2007) demonstrated. The proximity of the Gulf of Cadiz with the Sahara Desert favoured aeolian transport and deposition into the ocean. The Sahara is by far the largest hot desert on Earth (i.e., Itambi et al. 2009). During the Quaternary, the Sahara has represented a major source of fine particles, blown offshore to as far as the other side of the Atlantic Ocean and is currently the largest source of mineral aerosols globally (i.e., Itambi et al. 2009; Meinander et al. 2022; Vandorpe et al. 2022). Else, cold, and dry conditions involving major aeolian input characterise the HE as Rodrigo-Gámiz et al. (2011) shown.

Short-lived climatic events probably involved changes in the sediment supply to the continental shelf due to changes in erosion rates and river regimes of the river basin hinterlands (i.e., Lobo et al. 2001; Stumpf et al. 2011).

On the other hand, warmer periods are characterized by a lower supply of terrigenous material, but also by upwelling and a decrease in primary productivity (i.e., Brüchert et al. 2000; Colmenero - Hidalgo et al. 2004; Relvas et al. 2007; Vandorpe et al. 2022).

1.3.2 (Paleo)oceanographic conditions in SW Iberian continental margin

The Atlantic Meridional Overturning Current (AMOC) is a large-scale system of ocean currents that rotates water within the Atlantic Ocean, bringing warm water north and cold water south (i.e., Villanueva and Gutierrez-Mas 1994; Talley et al. 2011). The Gulf Stream (GS), a powerful ocean current that transports warm water from the Gulf of Mexico to the Atlantic Ocean, is included in the AMOC. One of its branches rotates with the Northeast trade wind and sweeps the Peninsula's coast to the south, from Galicia to Cape São Vicente. It is the Portuguese watercourse that flows from the

Gulf of Cadiz to the Canary Islands to the southwest (i.e., Colmenero-Hidalgo et al. 2004; Ferreira et al. 2008; Salgueiro et al. 2014; Vandorpe et al. 2022)

According to Salgueiro et al. (2014), the sea surface temperature (SST) reconstructions for the Last Glacial Maximum (LGM) suggest a significant cooling in the Atlantic Ocean-basin, resulting in a 30-40% decrease in the AMOC. While the cooling was stronger in the western Atlantic basin than in the eastern, the Gulf of Cadiz was especially prone to shifts in oceanographic conditions.

The observed SST and high export productivity in the Gulf of Cadiz indicate that the region has been continuously influenced by the subtropical Paleo-Azores Current during the LGM, which is consistent with the proposed extension of the Azores Front into the Gulf of Cadiz (i.e., Rogerson et al. 2004; Salgueiro et al. 2014). The Azores Front does not currently extend into the Gulf of Cadiz, but during the LGM and the YD, the front extended eastward into the Gulf of Cadiz, as Rogerson et al. (2004) stated.

Also, a rise in productivity on the South Iberian margin during HE has been noticed, which is link to nutrients advection along an Azores-like Front system (i.e., Rogerson et al. 2004; Salgueiro et al. 2014). Rogerson et al. (2004) observed intense scenarios along the western Iberian border, as well as a southern sector with milder temperatures, most likely because of local surface currents (especially the Azores Current) during HE.

The current oceanographic circulation in the Gulf of Cadiz is dominated by the exchange of water masses between the Atlantic Ocean and the Mediterranean Sea (i.e., Villanueva and Gutierrez-Mas 1994; Wienberg et al. 2010). In fact, as shown in Figure 4, several oceanographic pathways are present in the Gulf of Cadiz today, such as the Mediterranean Outflow Water (MOW), the Eastern North Atlantic Central Water (ENACW) and the North Atlantic Deep Water (NADW).

The ENACW (illustrated by thin white arrows in the Figure 4) crosses the PB from north to south and was defined as a southward flowing cold nutrient-rich subpolar component by Nichols et al. (2020), that circulate around 600 m water depth, in the Gulf of Cadiz. As Eynaud et al. (2009) established, the upwelled waters are sourced from the Eastern North Atlantic Central Water (ENACW) and, to a lesser extent, the Mediterranean Outflow Water (MOW). Seamounts (like Portimão Bank) are suitable topographic features for upwelling because cold nutrient-rich waters easily move upslope.

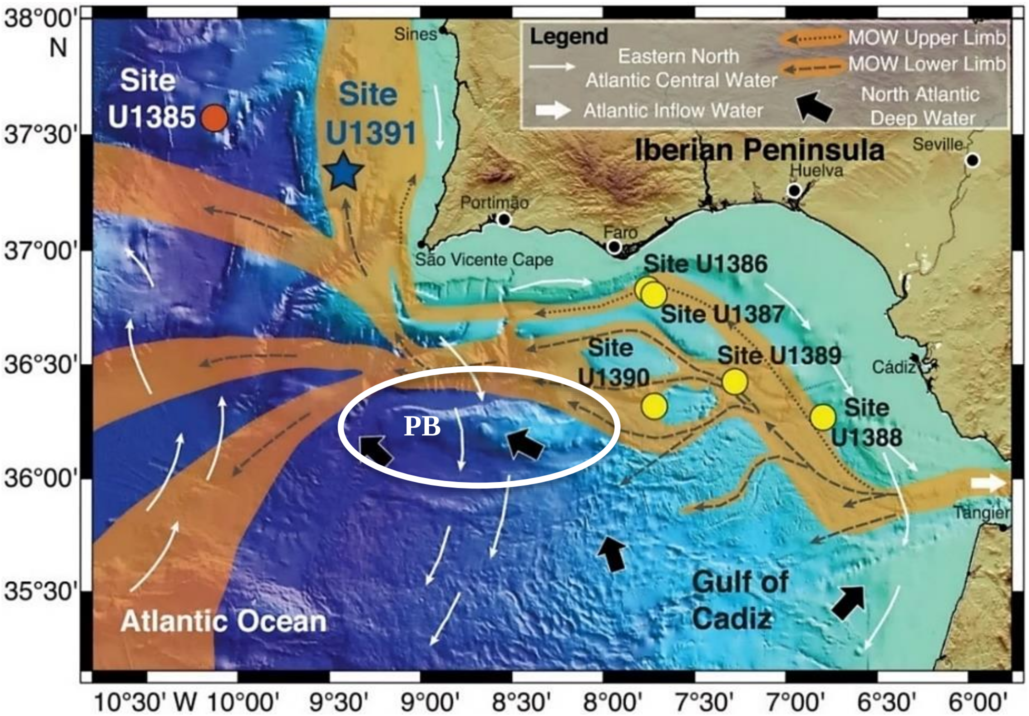

Figure 4. Main oceanographic pathways present today in the Gulf of Cadiz and potentially influencing the Portimão Bank (PB) circled in white (extracted from Nichols et al. 2020).

The MOW, a saline and warm water mass that typically flows northward beneath the ENACW from 500 down to 1500 m water depth (represented in orange in the Figure 4), passes north of the Portimão Bank (PB). The velocity of the MOW is strongly influenced by seafloor morphology. When the MOW is confined laterally, it accelerates, and decelerates when it spreads. The MOW has a large influence on sedimentation in the Gulf of Cadiz as it reworks silt carried by rivers into the gulf (i.e., Mulder et al. 2006; Marchès et al. 2007).

As Stumpf et al. (2011) demonstrated, the assemblages of marine sediments on the SW Iberian shelf have been influenced by contributions from various sources, such as suspended particulate matter (SPM) carried by the MOW, which enters the eastern North Atlantic through the Strait of Gibraltar and spreads at intermediate depths in the Gulf of Cadiz and along the Portuguese continental margin (or North African dust and river-transported particles from the Iberian Peninsula). The MOW has been active since the early Pliocene when the Messinian salinity crisis flooded the Mediterranean basin as Mulder et al. (2006) demonstrated. During cold events (see Table 1), the MOW circulation was intensified and spread to deeper levels in the water column than it is today. (i.e., Colmenero-Hidalgo et al. 2004; Llave et al. 2006; García et al. 2020).

Indeed, it was the case during the LGM, the MOW became denser (saltier) and settled deeper in the water column (i.e., Voelker et al. 2007; Nichols et al. 2020; García et al. 2020). As the seawater gets saltier, its density increases, and it starts to sink. Changing the density of a water mass perturbs the global circulation and the velocity of the currents. Changes in the current speed of MOW control the distance over which the clay-size particles can be transported and changes of the depth of the MOW layer inhibit or enable the deposition of SPM contributed from the Mediterranean Sea at a particular location (i.e., Colmenero-Hidalgo et al. 2004, Stumpf et al. 2011; Nichols et al. 2020; García et al. 2020).

Moreover, there is a strong winnowing produced by the MOW, washing out the fine particles (clay and coccoliths) and thereby concentrating the coarser ones (planktonic and benthic foraminifera, and silty or sandy terrigenous material) (i.e., Colmenero-Hidalgo et al. 2004; Ferreira et al. 2008; Mestdagh et al. 2019; García et al. 2020).

The NADW (shown by black arrows in the Figure 4) crosses the PB from southeast to northwest, and normally circulates below 1000 m water depth and can reach 3500-4000 m water depth in the Atlantic Ocean's deepest portion. According to Talley et al. (2011), the NADW is a notable layer of high salinity, high oxygen, and low nutrients.

1.4 Geological settings of the study area

The Gulf of Cadiz is a wide embayment of the Northeast Atlantic Ocean along the southwest coast of the Iberian Peninsula, extending for about 320 km from Cape São Vicente (southwest of Portugal) to the Strait of Gibraltar (see Figure 5). Currently, the Gulf of Cadiz is part of the passive Iberian continental margin as Terrinha et al. (2009) stated. The evolution of this margin has been more complex than that of other North Atlantic margins, as it is located at the eastern end of the Azores-Gibraltar transform fault and straddles the boundary of the African and Eurasian plates (i.e., Habgood et al. 2003; Terrinha et al. 2009; Roque et al. 2016; Silva et al. 2020).

The western part of the Gulf of Cadiz presents numerous geomorphological structures such as seamounts like the PB, canyons and channels, deep valleys, drifts, and abyssal plains (i.e., Mulder et al. 2006; Silva et al. 2020). The deeper basin of the Gulf of Cadiz is characterized by a generalized presence of diapiric ridges and mud volcanoes. It has long been recognized as a potentially hazardous area due to seismogenic and tsunamigenic activity, and slope instability (i.e., Wienberg et al. 2010; Silva et al. 2020).

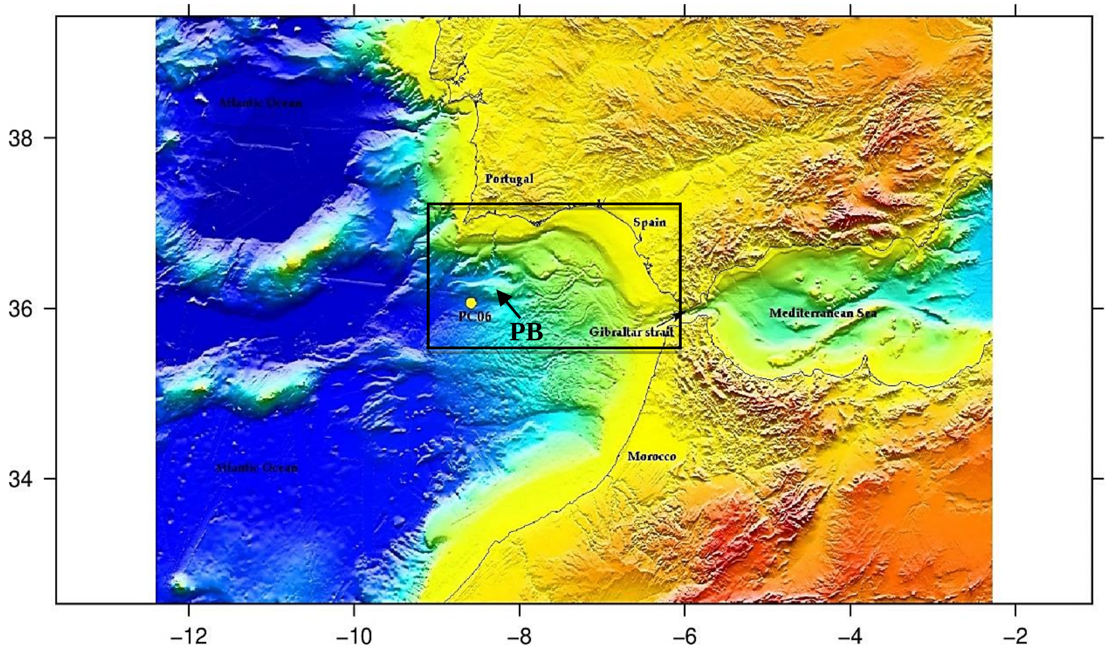

Figure 5. Bathymetric map of the Gulf of Cadiz (framed by the black rectangle). The piston core PC06 is represented by the yellow circle. The black arrow is pointing Portimão Bank (PB). The map was made using the software Mirone, and the data were extracted from the NOAA website. The Coordinates Reference System (CRS) is Pseudo-Mercator/EPSG: 3857.

The Portimão Bank (PB) is located near the continental slope of the southern Portuguese margin, about 100 km from the coast, in the Gulf of Cadiz (see Figure 5). The Portimão Bank stands at 1500 m water depth, has an elongated shape, and occupies an area of about 1800 km^2. It is 93 km long and 15-28 km wide, with a 12° maximum slope gradient (see Table 2). The top increases in depth towards the west, from 1500 to 3500 m. PB was formed during the Mesozoic rifting as a graben bounded by E-W normal faults. Structurally, the PB has been interpreted by Terrinha et al. (2009) as a pop-up structure, related to thrust faults resulting from the tectonic reversal of Mesozoic rift faults with marked diapiric activity. It corresponds to one of the main locations of the seismicity cluster in the Gulf of Cadiz (i.e., Terrinha et al. 2009; Fernández-Puga et al. 2014; Vazquez et al. 2015; Silva et al. 2020).

The primary morphological traits discovered on this bank are depicted in Figure 6. It consists of morphological features of tectonic and sedimentary origin. The tectonic features comprise reverse faults and ridges; the morphosedimentary features include mass movement and mixed features, such as depressions, bulges, domes on top, landslide scars and mass movement deposits, and flank scarps (i.e., Fernández-Puga et al. 2014; Vazquez et al. 2015; Roque et al. 2016; Silva et al. 2020).

Table 2. Summary of the location, geometric parameters (depth, length, width, height, area, and slope gradient) that characterise the Portimão Bank (modified from Vazquez et al. 2015).

Location		Latitude	Longitude	Max/Min water depth (m)	Length/ width (km)	Height (m)	Area (km^2)	Max/Min slope (°)
SW Iberia	Gulf of Cadiz	36°12,55 N	8°39,34'W	3800-3200	93/18-25	400-900	1800	12/0,01

The PB plays an important role in modifying deep sedimentary and oceanographic processes due to its geographic location (i.e., Mulder et al. 2006; Fernández-Puga et al. 2014; Vázquez et al. 2015; Silva et al. 2020) because it constitutes a barrier to the flow of sediments supplied by the Portuguese margin mainly through the Portimão and Faro canyons (see Figure 6), and it forms a topographic high that restricts oceanographic pathways (see Figure 4).

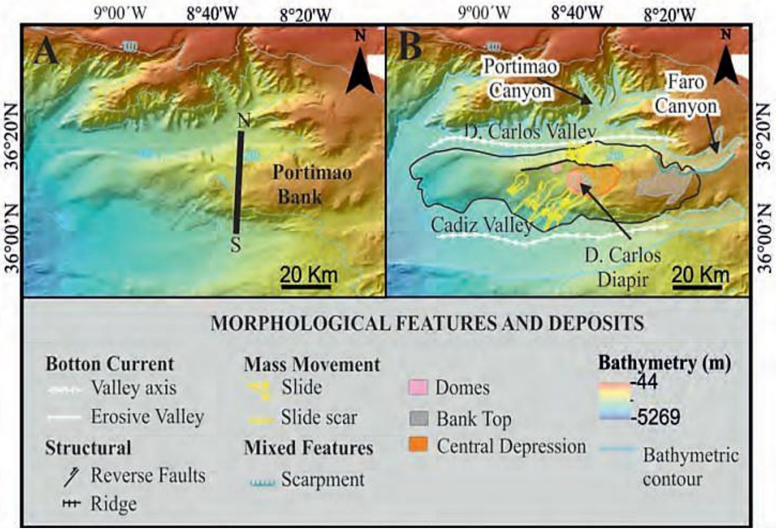

Figure 6. The Portimão Bank in the Gulf of Cadiz (SW-Iberian margin): (A) Bathymetric map, (B) Geomorphological map showing the main structural, mass-movement, mixed, and bottom current features (modified from Vazquez et al. 2015).

1.5 Objectives

In the scope of paleoenvironmental research, the PC06 core extracted from the depths of the abyssal plain southwest of the Gulf of Cadiz, specifically at the base of the Portimão Bank, represents a compelling yet underexplored repository of historical data. Our primary objective in this study is to conduct a comprehensive analysis of this sedimentary core, spanning the past 49,000 years, with a dual focus: firstly, to discern the key paleoenvironmental transformations imprinted within the core, and secondly, to unravel the origin and nature of the black lenticules interspersed throughout the core's stratigraphy.

By applying a multidisciplinary study, including sedimentological, mineralogical, and geochemical analyses, this will allow us to identify their source(s), the associated depositional processes and their paleoenvironmental implications for a period still understudied.

In the context of our work, a pivotal question looms large: To what extent can we attribute the overarching concepts of sedimentation processes, climatic dynamics, and oceanographic influences as the exclusive drivers behind these sedimentary deposits? Or should we consider the potential influence of localized, region-specific factors, particularly those centred around the Portimão Bank within the Gulf of Cadiz?

This study endeavours to contribute to the understanding of the geological history in the Gulf of Cadiz, within a temporal context back to thousand years ago. Through the integration of comprehensive analytical methodologies, our research aims to address these fundamental inquiries and unravel the complex interplay of factors that have shaped the environmental history of this region.

2 MATERIAL AND METHODS

2.1 Data set: PC06 deep-sea core

During the MONTERA-0412 scientific cruise, conducted in the Gulf of Cadiz (see Figure 4), a seismic survey, water samples, and several sedimentary cores have been collected with B/O SARMIENTO DE GAMBOA, between 23rd of April and 15th of May 2012, and briefly described (i.e., Vázquez and Alonso 2012).

One of these cores, the piston core PC06, was recovered on May 3, 2012, at 36°03.52' N/8°52.47' W at the base of the Portimão Bank (see Figure 7), at 3520 m water depth. It is 324,5 cm long, and has many parts with very intense black lenticules that had not previously been studied.

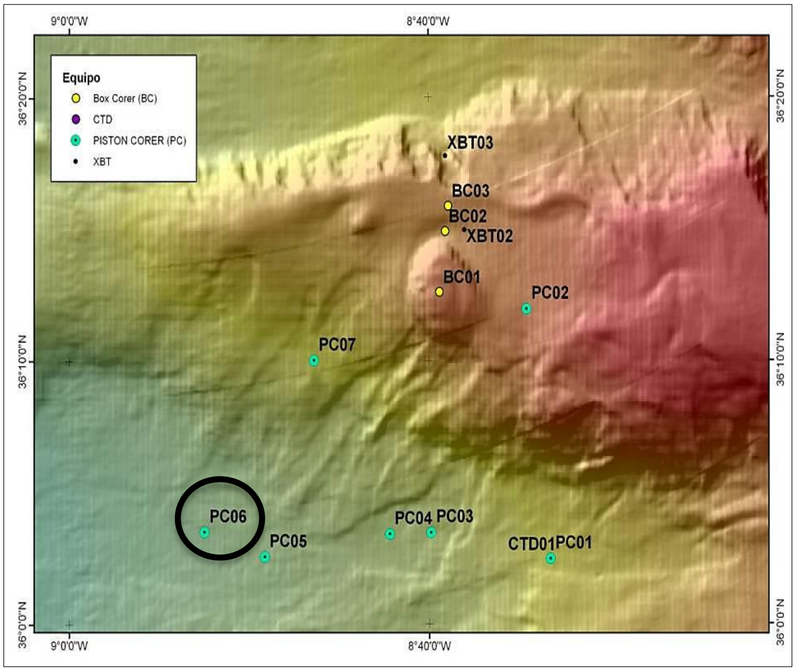

Figure 7. Bathymetric map of the Portimão Bank showing the exact location of the core PC06 (extracted from Vázquez and Alonso 2012). PC06 is represented on the left-bottom corner by the green dot circled in black, at the base of the Portimão Bank.

The core PC06 was opened, photographed (using a Multisensor core logger–MSCL), and described directly on board by the MONTERA research team (see Table 3). The first stage of our work was to fully understand these data (see Table 3) to gradually integrate it with newly obtained data.

Table 3. Synthetic table presenting the type of data already acquired, the methodology (X-rays stand for X-ray radiography, XRF means X-ray fluorescence spectrometry and MSCL stand for Multisensor core logger) used to obtain these data, where was it performed, the team (and/or person) in charge of the work, as well as the work we did with these data for our study.

DATA	METHOD	SAMPLING RESOLUTION	LOCATIONS	TEAM IN CHARGE	PRESENT WORK
Internal structure	X-Rays	High-resolution photographs	On board B/O SARMIENTO DE GAMBOA	MONTERA research team members	-
Magnetic susceptibility	MSCL	338 measurements			-
Photos		High-resolution photographs			Imagery analysis, and interpretation
Colour		49703 measurements			-
Geochemical contents	XRF	4890 measurements	CORELAB Barcelona University, Spain		Interpretation
Grain-size	Laser diffraction	55 samples	Institut de Ciències del Mar (ICM) Barcelona, Spain	MONTERA research team members	Statistical analysis, and interpretation
Datations	From ^{14}C	5 samples	Barcelona's Poznań Radiocarbon Laboratory	Age-depth model realised at IPMA Algès	Interpretation
Carbonates	Volumetric method of Scheibler	55 samples	Instituto Português do Mar e da Atmosfera (IPMA) Tavira, Portugal	IPMA	Interpretation
Organic matter	Loss on ignition	55 samples			
Smear slides	Sampled by hand	42 samples			Grains counting, statistical analysis, and interpretation (20 samples)
Sand	Sampled by hand	16 samples		Present work	Grains counting, statistical analysis, and interpretation

2.1.1 *Imagery analysis: General characteristics and bioturbation distribution*

The analysis of the core photo was focused on the colour change and other characteristics, and, on the black lenticules present along the core. For this part of the work, a visual analysis (U-channels were available at IPMA) and an image analysis (photographs of the U-channels) were carried out. U-channels were used (not high-resolution photos) because the black lenticules are much more visible on the fresh, smooth surface of the channels. However, the fresh sediments (from the U-channels) were already well oxidized, which is why only the photo analyse is presented. The colour of the sediments was described according to the Munsell chart reference.

For the bioturbation analysis, the high-resolution photographs from the PC06 core, took after the core opening, were digitally treated using the GNU Image Manipulation Programme (GIMP). According to Dorador and Rodriguez-Tovar (2014) investigations, a variety of adjustments (brightness, levels, curves, exposure, vibrance, saturation, and colour balance) have been reviewed on digital pictures to establish their usefulness for boosting trace fossil visibility. The most helpful changes were identified after application to multiple and varied examples with differences in ichnological (types of traces, size, filling material) and sedimentological features (lithology, particle size, colour).

The types of trace fossils discovered along the PC06 core were compared to the outcomes of Dorador and Rodriguez-Tovar (2013) and, Gingras et al. (2014).

2.1.2 Sedimentological analysis

Grain-size analyses were performed using a Coulter LS 100 laser particle size analyser at the Institut de Ciències del Mar (Barcelona) by our colleagues. This equipment measures particle size using the laser diffraction method (see Table 3), which is based on an optical principle that states that small particles in the path of a light beam scatter light in a particular symmetrical pattern that can be viewed on a screen. The particle size distribution can be derived from a certain pattern of scattered light intensity as a function of angle relative to the incident beam axis (‘flow pattern’) (© Coulter International Corporation, 1996).

At Portuguese Institute for Sea and Atmosphere (Tavira), the core was described and sampled for the following analyses: carbonates and organic matter measurements following the Scheibler method, and Loss on Ignition (LOI) method, respectively. Smear slides were also taken at specific intervals, especially in the dark lenticules (see Table 3). Carbonate content was estimated with an Eijkelkamp calcimeter, which treats samples with hydrochloric acid and makes a volumetric determination of the released CO_2. Organic matter was quantified by the method of loss on ignition (LOI), where about 200 mg of dry sediment was burned in a furnace at 450 °C for 2 hours (i.e., Roque et al. 2016; Silva et al. 2020)

2.1.3 Mineralogical analysis

2.1.3.1 Sand fraction

The analysis of the sand fraction (2mm - 63 μm) composition was therefore carried out on 16 selected samples (10 from the background sediments and 6 from the black lenticules).

First, we used a 63 μm sieve to separate the sands from the fine fraction (silt and clay). Then the samples were dried in the appropriate equipment (oven) at 40°C overnight. After, each sample was separated using sieves of different sizes: 500 μm, 250 μm and 125 μm, respectively. Finally, the samples of the 250 μm and 125 μm fractions (fine sand) were analysed under a binocular microscope (Leica EZ4W). It was decided to analyse these two fractions because given the very fine size of the sediments which make up core PC06, it is not relevant to study fractions >250 μm. Fraction <125 μm, however, is too small to be qualitatively observed with a binocular microscope.

In fact, 100 grains were counted (it has acceptable statistical accuracy, see the Gazzi-Dickinson method) using a counter (Labolan cell differential counter) for each fraction, per sample (see Appendix A). Terrigenous components were classified as quartz, micas, and rock fragments (other terrigenous). Biogenic components were classified as planktonic foraminifera (entire and fragments), benthic foraminifera, aggregates, and biogenic fragments (other biogenic). We took care to weigh the empty material (cups and containers), then with the dry sediments, to obtain the exact weight of each sample.

2.1.3.2 Smear slides

Sets of layers were selected from each of the core sections, based on previous results. In the first approach, we only had background sediment samples in the first section of the core, which was not relevant to apply a statistical analysis. Indeed, we made two more smear slides (from the black lenticules) to improve the detail of our analysis.

Following Marsaglia et al. (2013) method, we used a toothpick and distilled water to break and create a diluted suspension of sediment on the slide. Then the samples were dried at 40°C and cooled before fixing the sediments with an optical adhesive.

In total, 20 smear slides (12 background sediments and 8 black lenticules) were observed using a petrographic microscope (Olympus BX51). The mineralogical composition of each sample was identified (i.e., Marsaglia et al. 2013) and quantified using the Glagolev-Chayes point-counting method. Similarly, to the sand analyse, 100 grains were counted using a counter (Labolan cell differential counter) in 5 defined zones (4 corners and middle) of the lamina, for each sample. Terrigenous components such as clay minerals (biotite and chlorite), quartz, and felspars, as well as opaque grains, and heavy minerals, have been identified in the selected smear slides (see Appendix B). Nannofossils (mainly calcareous), foraminifera, and few sponge spicule were also observed and classified as biogenic components. Finally, pyrite, iron (Fe) oxides, and glauconite were identified as authigenic components (see Appendix B). Because organic matter can be both terrigenous and/or biogenic (even authigenic), it was recognised and quantified separately.

Additionally, the identification of marine microfossil species has been performed according to Leckie et al. (2015). The descriptive sheets of the sediment smear-slide, extracted from Marsaglia et al. (2013), were complete and used to create a synthetic table presenting the grains counting (see Appendix B).

2.1.4 Geochemical analysis

Geochemical analysis was performed along core with an Avaatech X-ray fluorescence (XRF) core scanner operated at both 10 kV and 30 kV at the CORELAB of Barcelona University. The relative contents of aluminium (Al), silicon (Si), phosphorus (P), sulphur (S), chlorine (Cl), argon (Ar), potassium (K), calcium (Ca), titanium (Ti), vanadium (V), chromium (Cr), manganese (Mn), iron (Fe), rhodium (Rh), nickel (Ni), copper (Cu), zinc (Zn), gallium (Ga), germanium (Ge), arsenic (As), bromine (Br), rubidium (Rb), strontium (Sr), yttrium (Y), zirconium (Zr), and lead (Pb) elements were measured on the split core section at 1 cm intervals.

In the present study, different chemical element ratios were investigated to provide information on sedimentation and paleoclimatic and/or paleoceanographic conditions. Indeed, the following two chemical element ratios (Zr/Al and Si/(Si+Al)) are used to interpret oceanographic and environmental changes. The Zr/Al ratio has already been used as an indicator of bottom currents in other regions (i.e., Bahr et al. 2014; Stow et al. 2018) and the Si/(Si+Al) ratio, for dry and wet conditions at least in the Alboran Sea (i.e., Moreno et al. 2005; Fink et al. 2013). Additionally, the ratio of chemical elements Ca/(Ca+Fe) was added in the present work because it is indicative of paleoproductivity (i.e., López-González et al. 2013), as well as Br/Ti ratio as marine organic matter accumulation indicator, and the content relative bromine (Br) (in count per second, cps) which gives information on the content of marine organic carbon (i.e., Ziegler et al. 2008; Rothwell and Croudace 2015).

2.1.5 Statistical analysis

2.1.5.1 Distribution analysis

According to Hillaire-Marcel and De Vernal (2007), particle size analysis provides insight into a variety of aspects of deep-sea sediments, particularly the circumstances during depositional processes. Grain-size data have been regarded as the greatest predictor of relative flow speed because deep-sea sediments often display little features other than biological disturbance. In this context, distribution analyses were applied to the grain-size using GRADISTAT software (i.e., Blott and Pye 2001). It is a software that has been written for the rapid analysis of grain-size statistics from any standard measuring techniques, such as sieving or laser granulometry (i.e., Blott and Pye 2001). Indeed, statistical parameters as mean, mode, sorting, skewness, and others were calculated for each grain-size measurement.

The statistical analysis used was the “geometric method of moments” (in µm). In the present work, the statistical analysis focused on the average grain-size, standard deviation (σ–sorting), as well as skewness (Sk) and kurtosis (K) (see Appendix C). Sorting generally falls into seven categories (see Appendix C). The smaller the value of σ, the lower the degree of particle size dispersion within the sediment sample. The more concentrated the distribution is, better is the sorting (i.e., Xie et al. 2020). Asymmetry reflects size distribution characteristics, which fall into five categories (see Appendix C). The kurtosis coefficient (K) into five categories (see Appendix C) describes the degree of concentration of particles of different sizes relative to the average particle size (i.e., Xie et al. 2020).

In addition, the median particle diameter (D50) of the Folk and Ward (1957) classification was added to our study because it is an indicator for characterizing the intensity of the paleo-bottom current (i.e., Martorelli et al. 2021). In the results, it is considered that the clay percentage is below 4µm (inclusive). Finally, the classification of sediments was carried out according to Blott and Pye (2012).

2.1.5.2 Age-depth modelling

The PC06 core age-depth model is based on five radiocarbons (^{14}C) dating (see Table 4) from well-preserved monospecific samples of planktonic foraminifera (*Neogloboquadrina incompta* or *Globorotalia inflata*) measured by accelerator mass spectrometry (AMS). The analysis was performed at the Poznań Radiocarbon Laboratory (see Table 3). The calibrated age model was created in the R environment (R Development Core Team, 2022) by Dra. Filipa Naughton, using the open-source program Clam 2.2 (i.e., Blaauw 2010). Clam 2.2 incorporates the most recently calibrated marine curve (‘Marine 13’) (i.e., Reimer et al. 2013).

Although reservoir ages have varied in the past, particularly during the last deglaciation (i.e., Siani et al. 2001; Waelbroeck et al. 2001; Stern and Lisiecki 2013), no adjustments to the reservoir ages integrated in the 'Marine' calibration data were made (data accuracy) (i.e., Reimer et al. 2013). The marine dataset (‘Marine 13.14c’) uses the global marine age reservoir correction (∆R) of 400 years for the Iberian margin as proposed by Bard et al. (2004). The interpolated age-depth model is given by a smoothed cubic spline curve (see Figure 8). All reported ages correspond to BP (before present: 1950 AD).

Table 4. Radiocarbon ages of PC06 deep-sea core. The depth intervals are expressed in cm below seafloor (cm BSF), the conventional AMS (accelerator mass spectrometry) ^{14}C ages and the error are in years (yrs.). Calibrated (Cal.) ages are expressed in year before present (BP).

Lab. code	Core depth (cm BSF)	Material	Conventional AMS ^{14}C ages BP (yrs.)	Error (yrs.)	Cal. BP median probability (yrs.)
Poz-67478	23	Foraminifera	3430	35	3301
Poz-70231	71	Foraminifera	11660	60	13150
Poz-70233	153	Foraminifera	19390	190	22898
Poz-75517	190	Foraminifera	20950	190	24760
Poz-75518	261	Foraminifera	28310	630	32045

2.1.5.3 Multivariate analysis

First, the data were checked using R software (R Development Core Team, 2022), to test the linearity and collinearity of the data. Then, a multivariate analysis (Principal Component Analysis, PCA) was carried out on the few components of the sand (planktonic and benthic foraminifera, quartz and other terrigenous) using two discrete variables (‘colour’ and fraction) (see Appendix H), because these components have a representative statistical correlation.

PCA technique looks for underlying gradients in the dataset to combine redundancies. In the end, items having similar proportional proportions of various variables are combined into a single set of principle components. The loading matrix and score matrix are two matrices that show the outcomes of the calculation. Each variable's loading has a value between -1 and 1. The proportion of the relevant principal component is indicated by this value, with values more than 0.4 being important. In other words, the results of a PCA are a two- or three-dimensional ordination graphic that approximates the continuum relationships between samples based on their similarity.

PCA was employed to compare background sediments and black lenticules composition identified in the 250 μm and 125 μm fractions.

2.1.5.4 Clustering analysis

A clustering analysis was performed on smear slides composition (see Appendix B) using the k-mean on R software (R Development Core Team, 2022). A set of 80 observations was divided into 2 groups by the k-mean clustering algorithm. Each cluster is distinguished by a centre point known as a centroid. In general, clustering is a technique that uses data patterns to assign comparable data points to groups. Algorithms for clustering identify comparable data points and group them into sets. In this study case, two groups (1) background sediments, and (2) black lenticules were analysed according to the % of clay, % of nannofossils, % of organic matter and % of pyrite. These specific components were selected after a visual evaluation of the mineralogical composition of the smear slides.

3 RESULTS

3.1 General characteristics of the core

PC06 is 324,5 cm long, with a gradual bedding contact, and sight changes in sediment's colour can be observed. From 324,5 up to 220 cm below seafloor (BSF) PC06 is dominated by black (N1) lenticules with background sediments light olive grey (5Y 5/2) (see Figure 8, 3/3). Then, between 220 and 75 cm BSF, the core is dominated by yellowish grey (5Y 7/2) background sediments and some black lenticules (see Figure 8, 2/3). Finally, from 75 up to 0 cm BSS, the core presents dusty yellowish (5Y 6/4) sediments without any black lenticules (see Figure 8, 1/3).

Figure 8. General characteristics of PC06. 'Zooms' in each section of the core were carried out at various intervals (1/3) 39-47 cm BSF, (2/3) 177-188 cm BSF, and (3/3) 271-284 cm BSF.

3.1.1 Trace fossils

According to the Bioturbation index (BI) card (see Appendix D), the core presents rare bioturbation. The greater BI (=2) is only detected in the top section of the core (between 66 and 0 cm BSF), which amounts to 6-30% bioturbated sediments on average (see Figure 9).

At least, three different types of trace fossils were identified throughout the core: *Thalassinoides*-like traces (see Appendix E and Figure 9, A.), *Taenidium*-like traces (see Appendix E and Figure 9, B.), and undefined bioturbation traces (see Figure 9, C.). Furthermore, subvertical burrows (see Figure 9, B.) and pyritized burrows (see Figure 9, D.) can be found in the core's last two sections (between 324,5 and 139 cm BSF). *Zoophycos*-like traces also seem to occur (see Appendix E), even though this has not been confirmed.

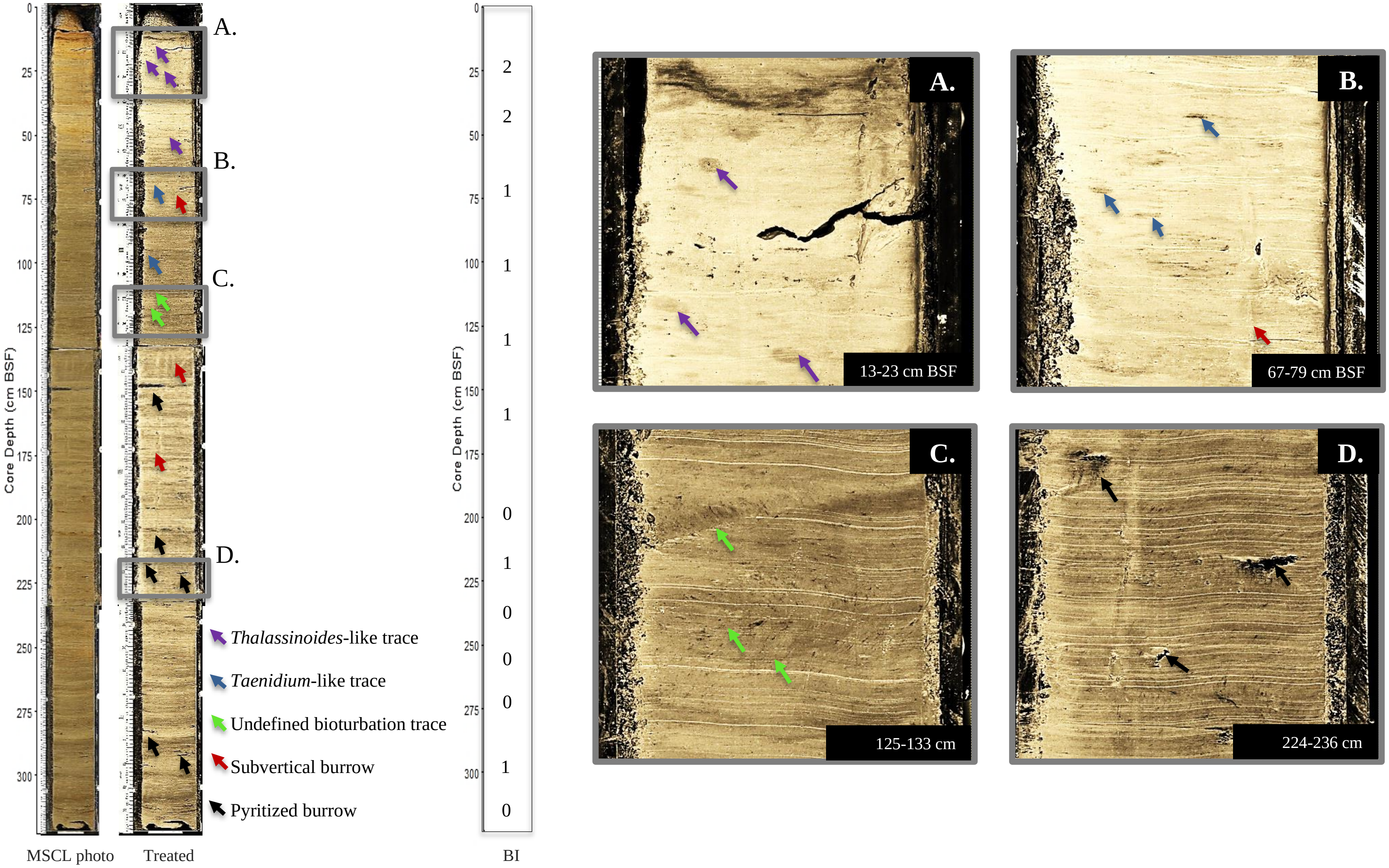

Figure 9. Bioturbations observed along the PC06 core after photo treatment. The purple arrows point to the *Thalassinoides*-like traces, the blue ones show the *Taenidium*-like traces, unidentified bioturbations in green, the subvertical burrow in red and the pyritized burrow in black. 'Zooms' of few of the mentioned traces were carried out at various intervals (A.) 13-23 cm BSF, (B.) 67-79 cm BSF, (C.) 125-133 cm BSF, and (D.) 224-236 cm BSF. The BI log also gives an estimate of the number of bioturbations along the PC06 core.

3.2 Type of sediments and stratigraphy

3.2.1 Sedimentological characteristics

According to the particle size classification of Blott and Pye (2012), the PC06 core is made up of mud, 52% silt and 46% clay (see Table 5). As shown in Figure 10, silt dominated the core between 324,5 and 75 cm BSF, while silt dominated between 75 and 0 cm BSF.

Five textural categories have been identified based on Blott and Pye (2012) classification: 1- slightly sandy clayey silt, (s)cSI; 2- very slightly sandy clayey silt, (vs)cSI; 3- clayey silt, cSI; 4- very slightly sandy silty clay, (vs)siC; and 5- silty clay, siC. The textural distribution of the sediments is consistent, with silt concentrations ranging from 45% to 55% (see Appendix F). From 324,5 to 225 cm BSF, the core is characterised by alternations of fine silt and fine clay, as seen in Figure 10. PC06 is dominated by a somewhat homogeneous mixture of (vs)cSI and cSI between 225 and 80 cm BSF. SiC and (vs)siC (finer clays) predominate between 75 and 20 cm BSF, while (s)cSI (coarser silts) is prevalent around 75 cm BSF (see Figure 10).

Additionally, the PC06 core has a mean grain size of about 3,99 μm (clay size), ranging from 2,70 μm to 6,28 μm (see Table 5). The mean grain-size increases from 324,5 (4 μm) to 305 cm BSF (6 μm), then decreases from 305 (6 μm) to 240 cm BSF (3 μm). Then, it remains stable from 240 to 125 cm BSF (around 4 μm), before increases again until 75 cm BSF (up to 6 μm). Finally, it decreases from 75 to 50 cm BSF (down to 3 μm) before increasing from 50 to 0 cm BSF (4 μm) (see Figure 10).

Table 5. Results of a basic statistical analysis performed on PC06 data for grain-size, texture (sand, silt, and clay content) and composition (organic matter–OM and calcium carbonates–CaCO3, content).

	Grain-size (μm)	**% Sand**	**% Silt**	**% Clay**	**% OM**	**% $CaCO_3$**
Mean average	3,99	1,85	52,13	46,02	6,40	25,14
Maximum	6,28	6,63	64,25	56,26	7,93	36,72
Minimum	2,70	0,05	41,50	34,05	4,62	17,76

The sorting (σ) seems to follow the profile of the average particle size. It remains stable (4,0-4,4) from 324,5 to 125 cm of BSF, then increases up to 75 cm of BSF (up to 5.2), decreases abruptly up to 50 cm of BSF (up to 4,0), before remaining stable from 50 to 0 cm BSF (4,4). As σ evolves between 4.0 and 5.2 (see Figure 10) along PC06, the sediments are all very poorly sorted (see Appendix C). Skewness (Sk) decreases from 324,5 (-0.3) to 305 cm BSF (-0,6), then remains stable up to 75 cm BSF (-0,3), increases from 75 to 50 cm BSF (0,0) and again remains stable up to 0 cm BSF (-0,2). Accordingly, the sediment distribution between 324,5 and 305 cm BSF is fine skewed, while the sediment distribution between 305 and 0 cm BSF is symmetrical (see Appendix C). Additionally, kurtosis (K) increases sharply from 324,5 to 305 cm BSF (from 2,60 to 3,25), remains stable up to 125 cm BSF (2,60-2,75), then increases from 125 to 110 cm BSF (up to 3,25), decreases again to 75 cm BSF (up to 2,50) before remaining stable from 75 to 0 cm BSF (2,70) (see Figure 10). As K evolves between 2,50 and 3,25 the sediment distribution is mesokurtic (see Appendix C) throughout the whole core.

Concerning the OM, it has an average content of approximately 6,4%, ranging from 4,6% to 7,9% (see table 5). The OM contents remain stable from 324,5 to 170 cm BSF (7,0-7,5%), with a peak around 175 cm BSF (7,9%), slowly decrease from 175 to 25 cm BSF (from 7,9 to 5,0%), finally increasing sharply to 0 cm BSF (from 5,0% to 7,9%) (see Figure 10). Additionally, the average calcium carbonate ($CaCO_3$) content of PC06 is approximately 25,1%, ranging from 17,8% to 36,7% (see Table 5). The $CaCO_3$ content decreases slightly from 324,5 to 310 cm BSF (from 23 to 17,8%), then increases up to 275 cm BSF (up to 30%) where it remains stable up to 100 cm BSF (approximately 25-30%), it decreases again from 100 to 80 cm BSF (from 28 to 17,8%), then increases sharply to 30 cm BSF, before slowly decreasing to 0 cm BSF (up to 25%) (see Figure 10).

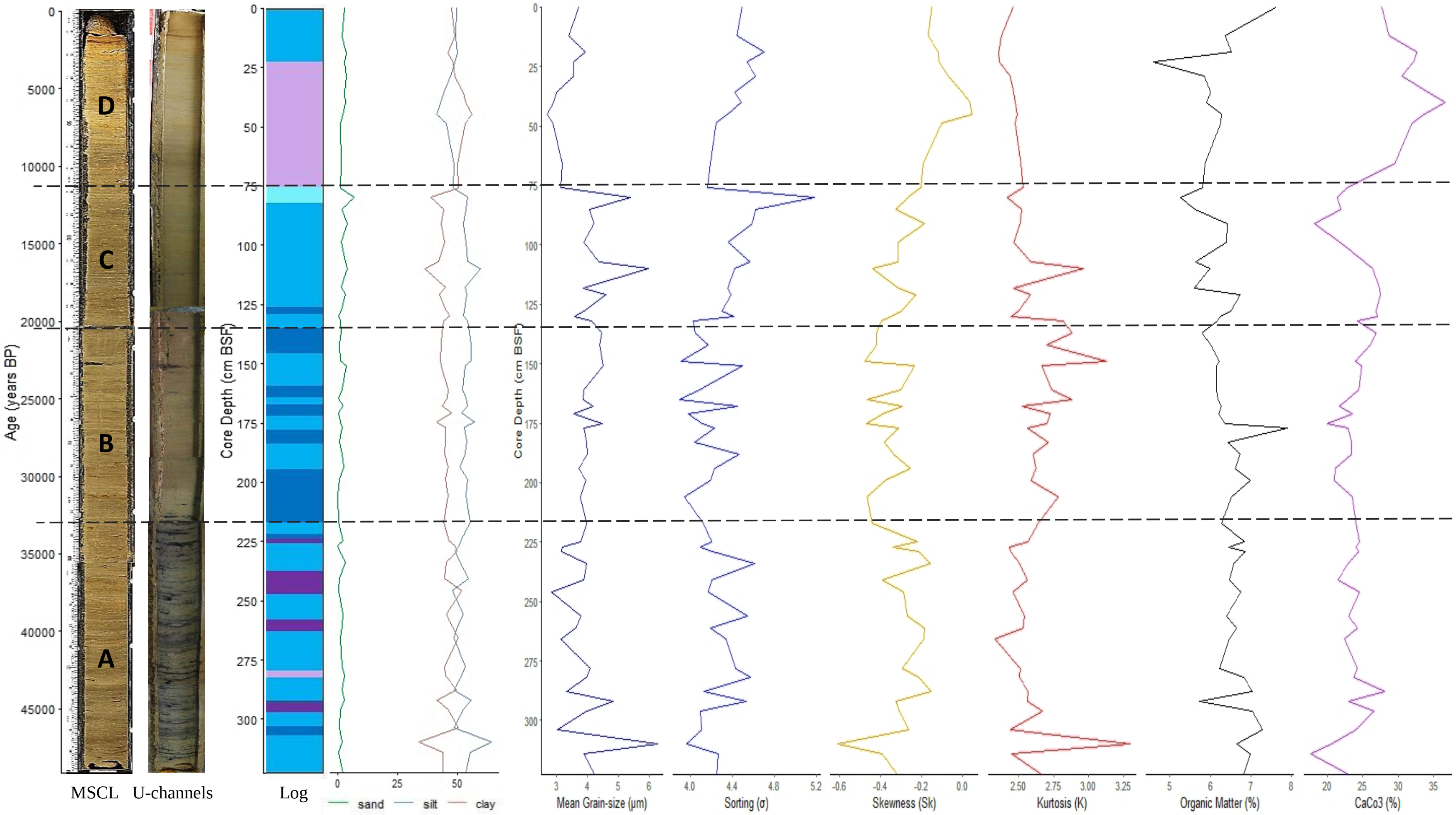

Figure 10. Vertical distribution of sedimentological data of PC06 including age (cal. years BP), photos (high-resolution from MSCL, and U-channels), sedimentary Log (Blott and Pye 2012), sand (in light green), silt (in light red), clay (in light blue) percentages, mean grain-size (dark blue curve), sorting (in blue), skewness (in yellow), kurtosis (in brown), as well as organic matter (black curve) and calcium carbonates–$CaCO_3$ (purple curve) contents. The three black dashed lines represent the boundaries between the defined sedimentary units: A/B 220 cm BSF (or 33807 cal. yrs. BP); B/C 132cm BSF (or 20937 cal. yrs. BP); C/D 75 cm BSF (or 11551 cal. yrs. BP). The data used comes from the acquired data presented in Table 3 (55 samples per data).

3.2.2 Mineralogical composition

3.2.2.1 Sand composition

For the 125 µm fraction, the quartz, micas, and other terrigenous components is represented by 31% along the entire core, and (benthic and planktonic) foraminifera, aggregates, and other biogenic components is 69%. It could be highlighted by the following characteristics:

Quartz (low content) was found at different levels throughout the core, particularly at 250 cm BSF cm (12.5%), 140 cm BSF (11%), and between 80 and 50 cm BSF (10.5%) (see Figure 11, A.). Micas (moderate content) show an increase around 150 cm BSF reaching 20%. Other terrigenouss (OT), such as oxidized grains (see Figure 12, B. and D.) (high content) are strongly present around 300 cm of BSF (>40%) (see Figure 11, A.).

Benthic foraminifera (moderate content) showed a peak at 220 cm BSF (20%). Planktonic foraminifera (high content) dominate the entire core, in a proportion between 40 and 60% (see Figure 11, A.). Aggregates (pieces of organisms supported by cement) (moderate content) show an increase between 100 and 50 cm BSF (>7.5%), as well as other biogenics (OB) (moderate) which rise up to 12.5% (see Figure 11, A.).

For the 250 µm fraction, the terrigenous component is represented at 21% over the entire core, and the biogenic component is at 79%. It could be supported by the following characteristics:

Quartz (low grade) was found at various levels throughout the core, particularly between 310 and 250 cm BSF cm (up to 9.5%), 110 cm BSF (8.5%) and peaks at 60 cm BSF cm (10%) (see Figure 11, B.). Micas (low content) show an increase around 300 cm BSF reaching 7%. OT (high content) are strongly present around 300 cm of BSF (>40%), and increase between 200 and 100 cm of BSF (between 20-25%) (see Figure 11, B.). Benthic foraminifera (moderate content) showed a peak at 110 cm BSF (10%). Planktonic foraminifera (high content) dominate the entire core, in a proportion between 40 and 60% (see Figure 11, B.). The aggregates (moderate content) show an increase of around 50 cm BSF (25%). OB, which rises up to 15% (moderate content), increases between 310 and 170 cm BSF (10-15%) and peaks around 80 cm BSF (10%) (see Figure 11, B.).

Biogenic components, essentially planktonic foraminifera, largely dominate the two sand fractions (250 and 125 µm) studied for the deep-sea core PC06.

Moreover, as illustrated in Figure 12, A. and C., the background sediments are dominated by biogenic components, mainly planktonic foraminifera (45–60%) in both the 250 µm and 125 µm fractions (see Figure 13, A., and C.).

The black lenticules also contain planktonic foraminifera (40-50%) as well as other terrigenous components (15-45%). This difference is more relevant in the 125 µm fraction (see Figures 12, B. and 13, B.) where the percentage ranges are larger (see Figure 13) and where the presence of unidentified grey minerals (classified as other terrigenous), as well as oxidized minerals, can be noticed with the binocular microscope (see Figure 12).

This could explain the fact that biogenic components, mainly planktonic foraminifera, dominate in the sand fraction of PC06. Indeed, black lenticules are not present throughout the whole core, and we must consider the number of samples studied (only 6 samples from black lenticules for 10 from the background sediments).

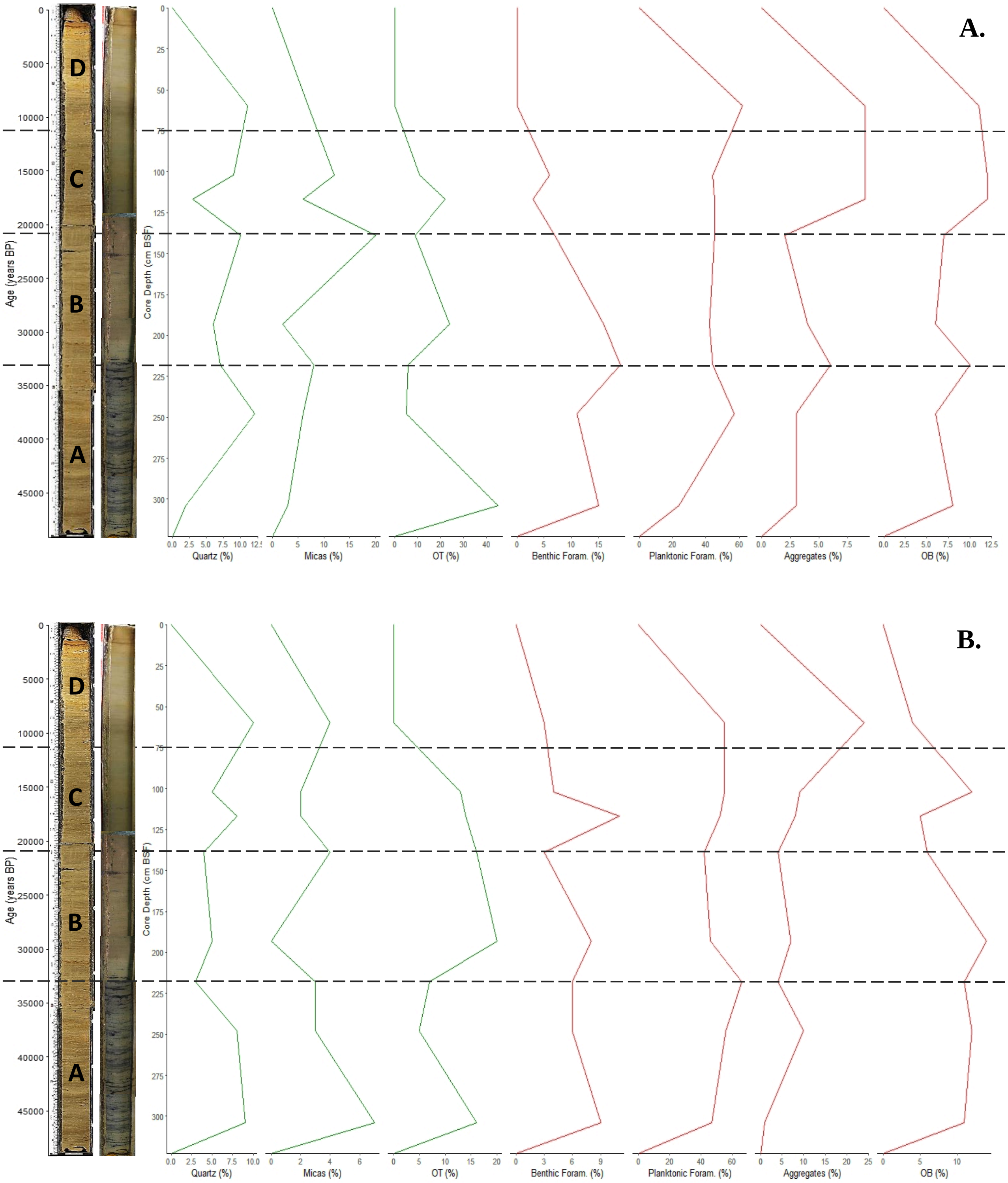

Figure 11. Vertical evolution of the sand mineralogical composition (in percentage) in the (A.) 125 µm fraction and (B.) 250 µm fraction using 16 samples. Quartz, micas and other terrigenous–OT are classified as terrigenous components (green curves), and benthic foraminifera, planktonic foraminifera, aggregates, and other biogenic–OB as biogenic components (red curves). The three black dashed lines represent the boundaries between the defined sedimentary units: A/B 220 cm BSF (or 33807 cal. yrs. BP); B/C 132cm BSF (or 20937 cal. yrs. BP); C/D 75 cm BSF (or 11551 cal. yrs. BP).

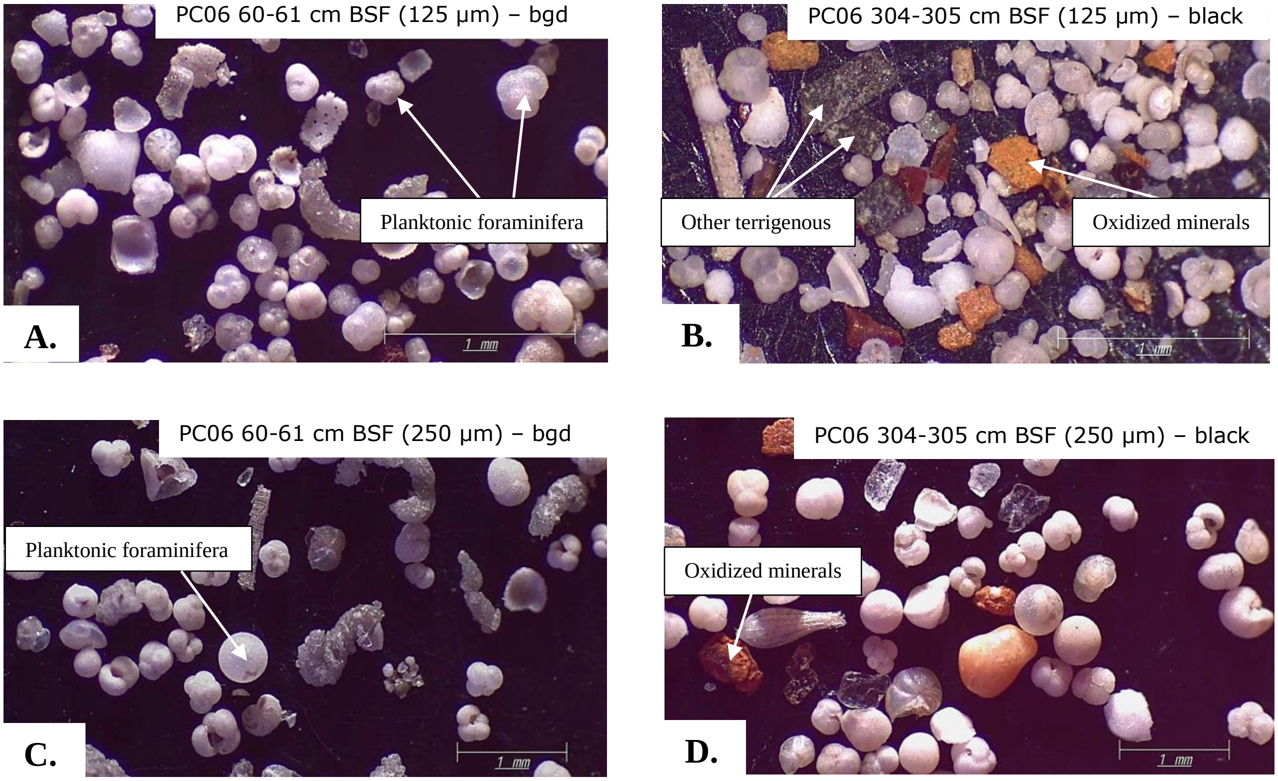

Figure 12. Photographs taken with a binocular microscope showing the mineralogical composition of (A.) background–bgd sediments, (B.) black lenticules both in the 125 µm fraction, and (C.) background–bgd sediments, (D.) black lenticules both in the 250 µm fraction.

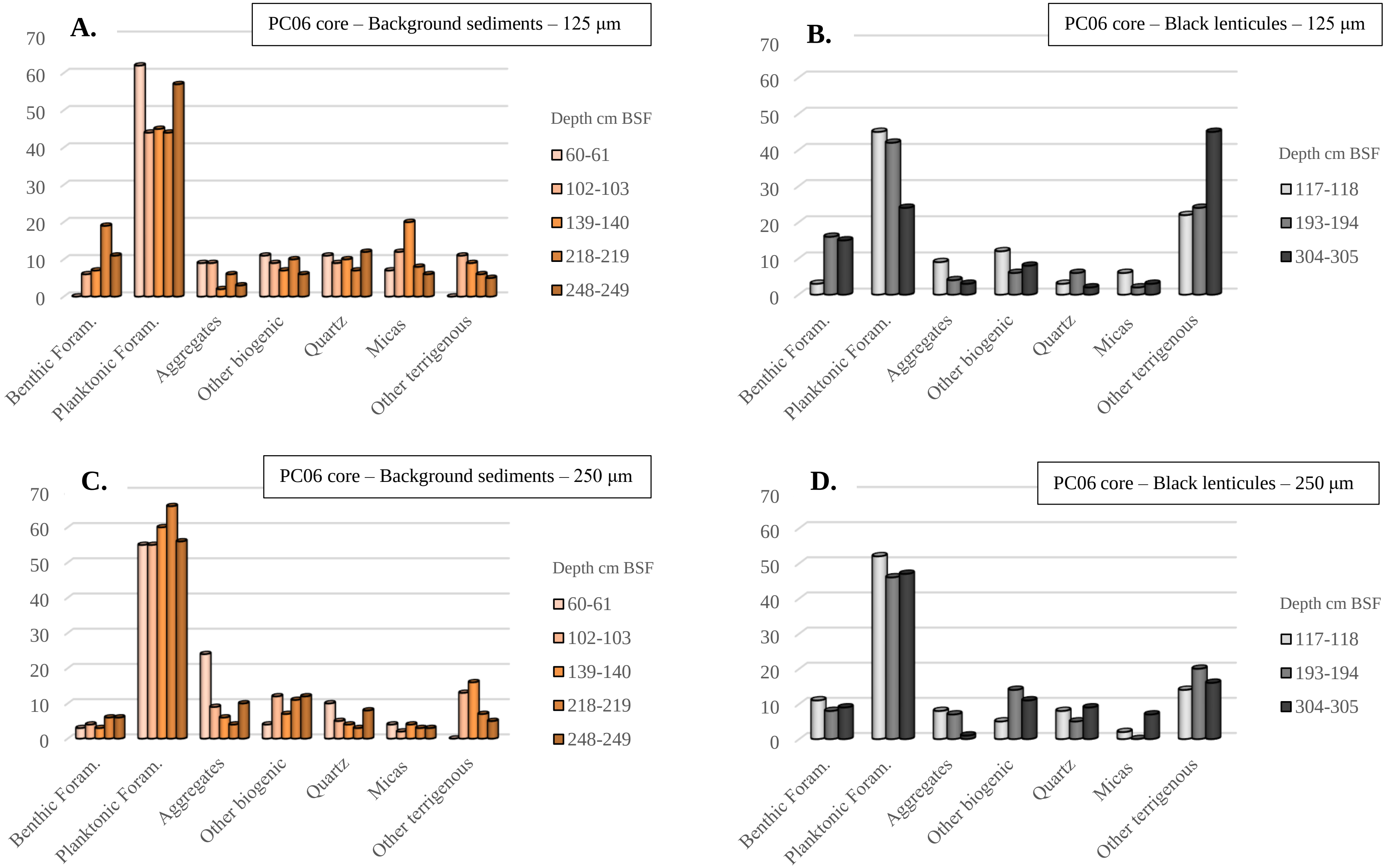

Figure 13. Statistical comparison between mineralogical composition of (A.) background sediments, (B.) black lenticules both in the 125 µm fraction, and (C.) background sediments, (D.) black lenticules both in the 250 µm fraction. The orange histograms represent the % (y-axes) of components (x-axes) in the background sediments (10 samples) and the grey the % of components in black lenticules (6 samples).

3.2.2.2 Smear slides composition

Terrigenous components make up 40% of the composition of the background sediment smear slides. Indeed, clay minerals (mainly biotite) dominate between 300 and 350 cm of BSF (25 to 30%) and between 145 and 25 cm of BSF (30%). They show a slight decrease between 110 and 150 cm BSF (<10%), mainly due to the increase in organic matter (>25%) (see Figure 14). Quartz (which varies between 5 and 15%) and feldspar (which varies between 2.5 and 5.5%) are not the most relevant of the terrigenous components, even if quartz presents a peak (20%) around 145 cm BSF, and feldspar increases (up to 7.5%) at approximately 25 cm BSF (see Figure 14). Opaque grains are strongly present around 275 cm BSF (up to 12.5%) and have a peak around 100 cm BSF (around 12%), but they remain rare for the rest of the core (see Figure 14). Heavy minerals are almost non-existent along the core but appear suddenly around 160-150 cm BSF with a fairly good content (>10%) (see Figure 14).

Concerning the biogenic components, which represent 30,5% of the composition of the smear slides, are mainly represented by nannofossils (mainly calcareous) which increase from 324,5 to 250 cm BSF (from 0 to 40%) before slowly decreasing to 150 cm BSF (at 0%), and finally increasing again up to 0 cm BSF, with the highest values (>60%) being between 80 and 20 cm BSF (see Figure 14). Foraminifera are rarer (which is rather in agreement with the size of the grains observed under the petrographic microscope) but are present around 150 cm BSF (up to 20%) as well as around 120 cm BSF (peak around 15%) (see Figure 14). It is better to refer to the sand results for foraminifera.

In addition, authigenic components (17,5% of the core), dominated by pyrite, mark three zones in the core: approximately 310 cm BSF (35% pyrite, 4% Fe oxides), between 250 and 150 cm BSF (20 to 40% pyrite, up to 15% Fe oxides around 210 cm BSF), and between 120 and 75 cm BSF (10-20% pyrite and 5-10% Fe oxides) (see Figure 14).

Finally, organic matter (12% of PC06 smear slide composition) peaks around 310 cm BSF (>20%), then dominates between 210 and 80 cm BSF (25%) and between 250 and 150 cm BSF (around 20%), as does pyrite at the same depths (see Figure 14).

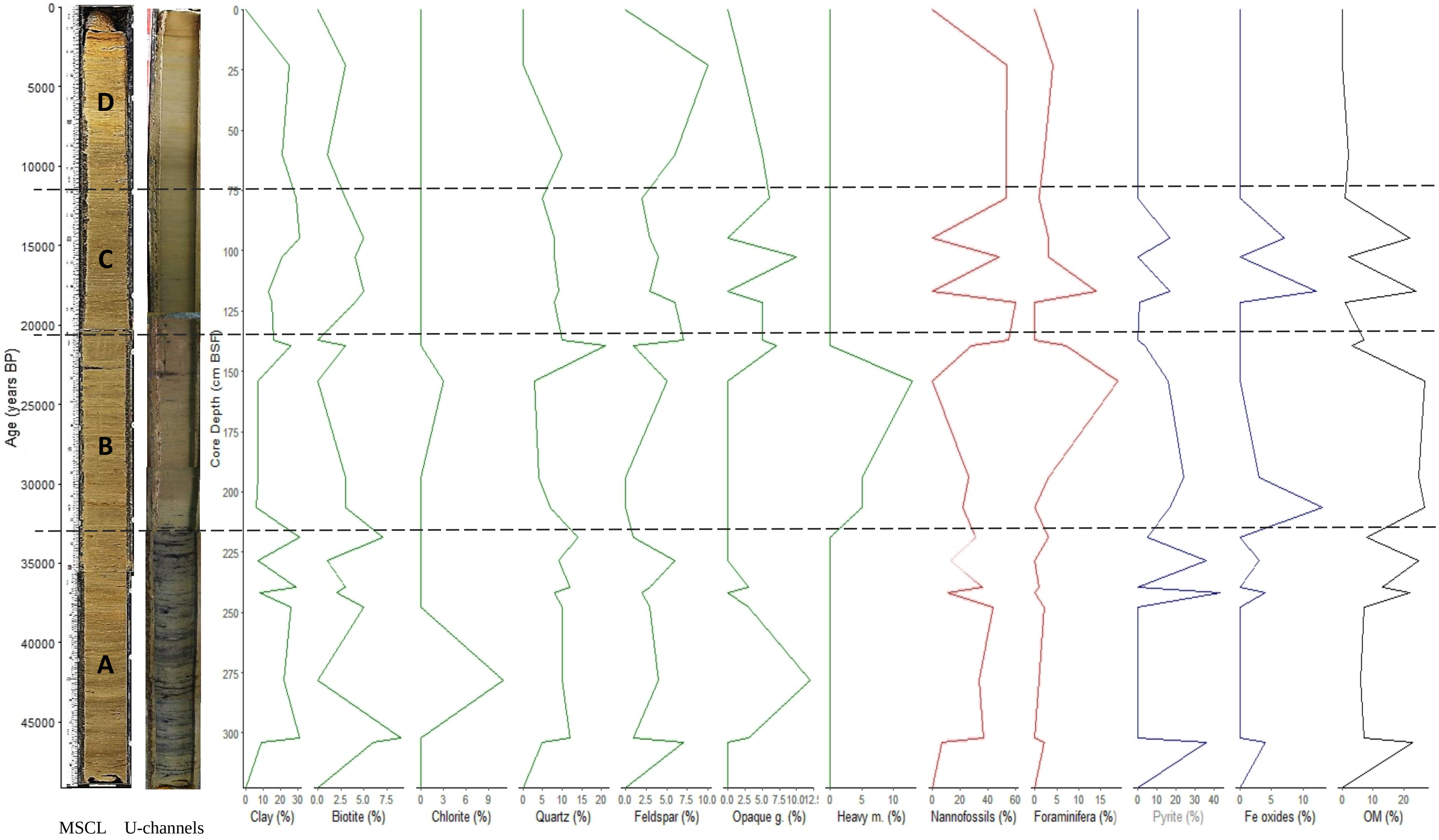

Figure 14. Vertical evolution of the mineralogical composition (in percentage) of the smear slides (20 samples) in the terrigenous components (green curves): clay, biotite, chlorite, quartz, feldspar, opaque grains, and heavy minerals; biogenic components (red curves): nannofossils and foraminifera; authigenic components (dark blue curves): pyrite and iron–Fe oxides; and organic matter–OM (black curve). Sponge spicule and glauconite are not represented less than 2% of the PC06 core mineralogical composition. The three black dashed lines represent the boundaries between the defined sedimentary units: A/B 220 cm BSF (or 33807 cal. yrs. BP); B/C 132cm BSF (or 20937 cal. yrs. BP); C/D 75 cm BSF (or 11551 cal. yrs. BP).

Table 6. The average content (%) in the terrigenous, biogenic, authigenic components, and organic matter in background sediments/black lenticules (20 samples–smear slides) from the PC06 deep-sea core (total grains counted: 2000).

Components (smear slides)			**Average (%)**			
			Background sediments		**Black lenticules**	
Terrigenous	Clay	Biotite Chlorite	29	**48**	13	**32**
	Quartz		10		7	
	Feldspar		4		3	
	Opaque grains		5		0	
	Heavy minerals		0		9	
Biogenic	Nannofossils		44	**46**	10	**15**
	Foraminifera		2		5	
	Sponge spicule		0		0	
Authigenic	Pyrite		1	**1**	26	**34**
	Fe oxides		0		6	
	Glauconite		0		2	
Organic matter			**5**		**19**	

Furthermore, as documented in Table 6, the background sediments are dominated by terrigenous (48%) components especially clay minerals (29%), closely followed by biogenic (46%) components predominantly nannofossils (44%) (see Figure 15). Concerning the nannofossils which constitute the marine muds of core PC06, they are essentially skeletons of calcareous coccolithophorids (see Appendix G). Under a petrographic microscope (polarized light microscopy - PLM), the calcium carbonate plates are plainly apparent (see Appendix G, photos). Several coccolithophores have been detected, with the major species being *Emiliania huxleyi*, *Reticulofenestra bisecta*, and *Reticulofenestra haqii.*

Smear slide samples contain coccolithophore species (see Appendix G) that are significantly older (Late Oligocene – 23.9 million years) than core PC06 (Late Pleistocene – 50 thousand years) itself.

Authigenic (1%) components are not representative of the background sediment's mineralogical composition unlike for the black lenticules, where authigenic (34%) components, mostly pyrite (26%), are dominant (see Figure 15). Dark lenticules are also composed of terrigenous (32%) components such as clay minerals (13%) and heavy minerals (9%). Organic matter is present both in small quantities in the background sediments (5%), and more abundant in the black lenticules (19%).

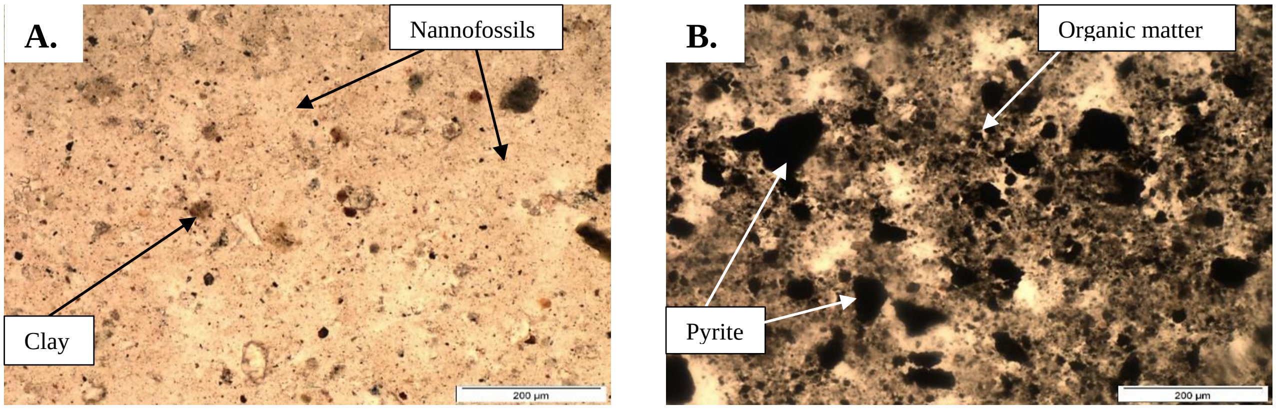

Figure 15. Plain light photographs taken with a petrographic microscope (10x eyepiece–20x objective lens) showing the mineralogical composition of (A.) background sediments and (B.) black lenticules. The arrows in both images indicate the main components that differentiate both.

3.2.3 Geochemical proxies

The ratio Zr/Al has an increasing tendency from 324,5 up to 132 cm BSF (from 1,00 to 1,75). Then, it remains stable until 75 cm BSF (around 1,25), before increasing again until 0 cm BSF (from 1,00 up to 2,00). Four main peaks are notable: one round 155 cm BSF (2,00), one around 60-65 cm BSF (up to 2,00), one around 45 cm BSF and one around 30 cm BSF (both up to 1,75) (see Figure 16).

The Si/(Si+Al) ratio has the same behaviour as the Zr/Al: an increase from 324,5 up to 132 cm BSF (from 0,905 to 0,915). Then, it remains stable until 75 cm BSF (around 0,10), before increasing again until 0 cm BSF (from 0,910 up to 0,920). Four main peaks are notable: one round 215 cm BSF (0,918), one around 155 cm BSF (up to 0,920), one around 60-65 cm BSF (0,919), and one around 45 cm BSF (0,915) (see Figure 16).

The Ca/(Ca+Fe) ratio evolves more than the two previous ones. It varies between 0,60 and 0,73 between 324,5 and 220 cm BSF. Then, it shows an increasing trend up to 110 cm BSF (from 0,70 to 0,75), before decreasing sharply from 110 up to 75 cm BSF (from 0,70 to 0,55). Finally, it slowly increases again to 0 cm BSF (to 0,80) (see Figure 16).

The Br/Ti chemical element ratio increases from 324,5 up to 225 cm BSF (from 0,08 to 0,16), before decreasing slightly up to 175 cm BSF (to 0,10). Then, it slowly increases from 75 to 0 cm BSF (from 0,10 to 0,24) with a peak (higher value) around 40-45 cm BSF (see Figure 16).

Finally, the chemical element Br follows the same behaviour as the Br/Ti ratio, with values ranging from 1,500 to 3,000 cps (counts per second) (see Figure 16).

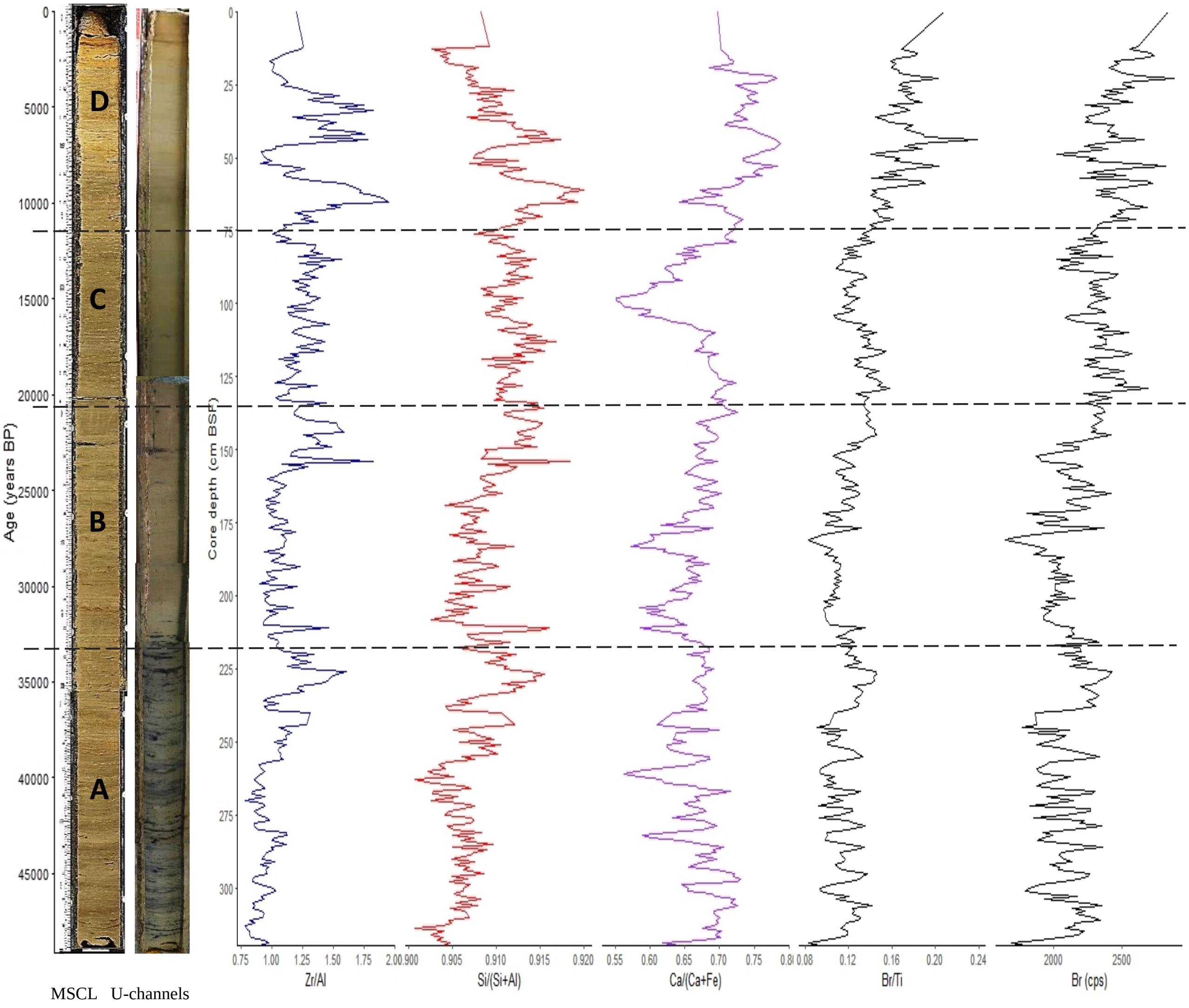

Figure 16. Vertical profiles of the chemical element ratios, Zr/Al; Si/(Si+Al); Ca/(Ca+Fe); Br/Ti, as well as Br chemical element, in counts per second (cps), including ages (cal. years BP) and photos. The three black dashed lines represent the boundaries between the defined sedimentary units: A/B 220 cm BSF (or 33807 cal. yrs. BP); B/C 132cm BSF (or 20937 cal. yrs. BP); C/D 75 cm BSF (or 11551 cal. yrs. BP).

3.3 Statistical analysis results

3.3.1 *Age-depth model*

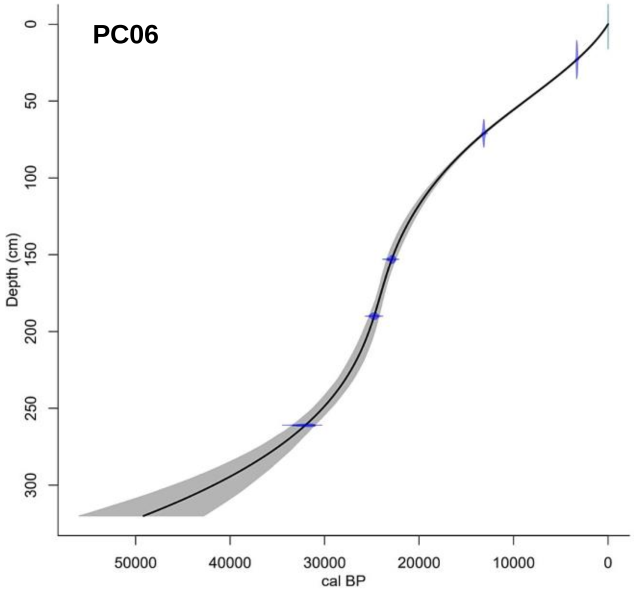

Results of the age-depth modelling of the core is displayed in Figure 17 and reflect increasing uncertainties with greater distance from calibrated sample ages (blue probability distributions).

It suggests a mean age of 49,171 years cal. BP. at the core base (324,5 cm BSF).

Figure 17. Age-depth model output of the PC06 core including calibrated ^{14}C ages (blue). The dark curve represents the single 'best' model based on the weighted mean age for each depth. The grey contours reflect the 95% confidence interval (minimum and maximum cal. BP ages).

3.3.2 *Correlation of sand composition*

As seen in Figure 17, PCA could only be applied on four variables: benthic foraminifera, planktonic foraminifera, quartz, and other terrigenous, because they present a statistically representative correlation (see Figure 18, red squares). We have some differences in our samples. First, for the 'colour' variable: it is statistically different for other terrigenous, and benthic foraminifera (see Figure 18, green squares) (even planktonic foraminifera). Second, for the fraction variable: it is statistically different for micas and planktonic foraminifera (see Figure 18, blue squares).

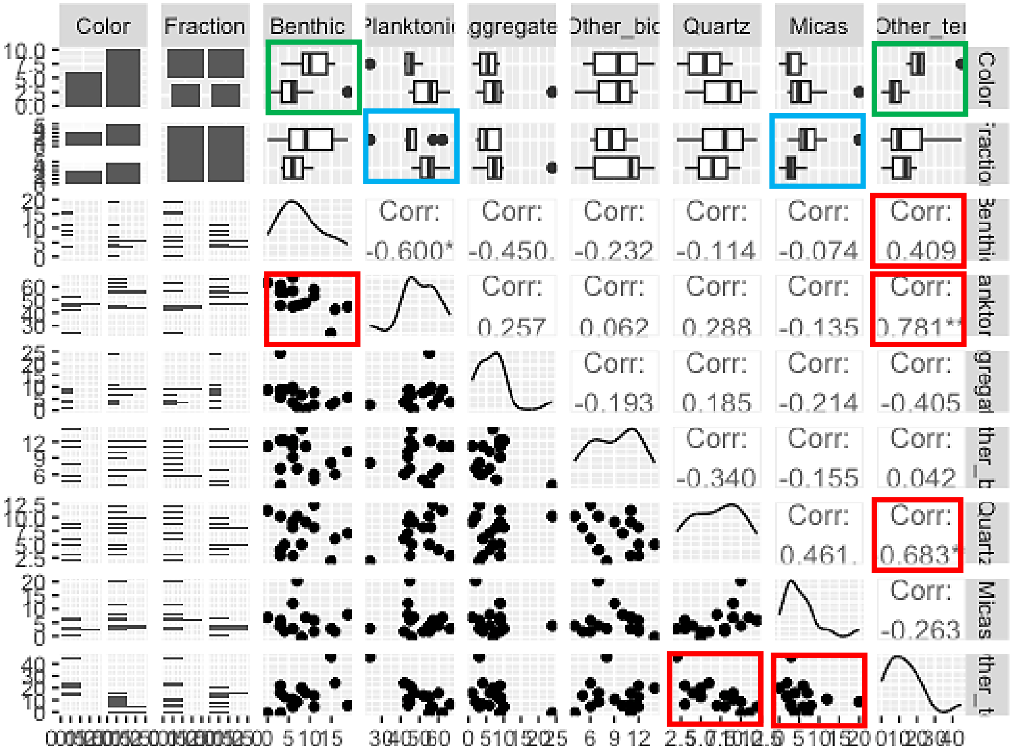

Figure 18. Pairplot presenting the main variables from the sand composition in two particle size fractions (125 µm and 250 µm) and the two identified sediment 'colours' (from the background sediments and the black lenticules). The Left panel presents the scatter plots or the histograms of the variables; the diagonal present the distribution curve for each variable, and the right panel presents either the correlation factor or conditional boxplots.

In the PCA biplots (see Figure 19, A., and B.), the 2 sections show different spatial distributions along the axes PCA 1 (Dim1) and PCA 2 (Dim 2). The background sediment samples (Figure 18, A., red dots) are mainly grouped on the negative side of PCA 1 (see Figure 19, A.) due to the higher number of planktonic foraminifera and quartz (see Figure 19, B.), sample number 11 being the only one on the positive side of PCA 1 due to the increases in benthic foraminifera in this sample. Black lenticules samples (Figure 18, A, black dots) are located on the positive side of the PCA 1 (see Figure 19, A.) due to the high number of other terrigenous components, and benthic foraminifera (see Figure 19, B.).

As the distribution of both background sediments and black lenticules cluster on both side of PCA 2 (see Figure 19, A.), there are no significant changes in the mineralogical composition regarding the fractions.

In the initial component assemblage visible in the 125 µm fraction (see Figure 19, A.), planktonic foraminifera (0,770) correlate to background sediments (or rest of the core) (0,832) (see Appendix L). Other terrigenous particles (0,935) correlate to black lenticules (1,387) in the 250 µm fraction's second component assemblage (see Appendix H).

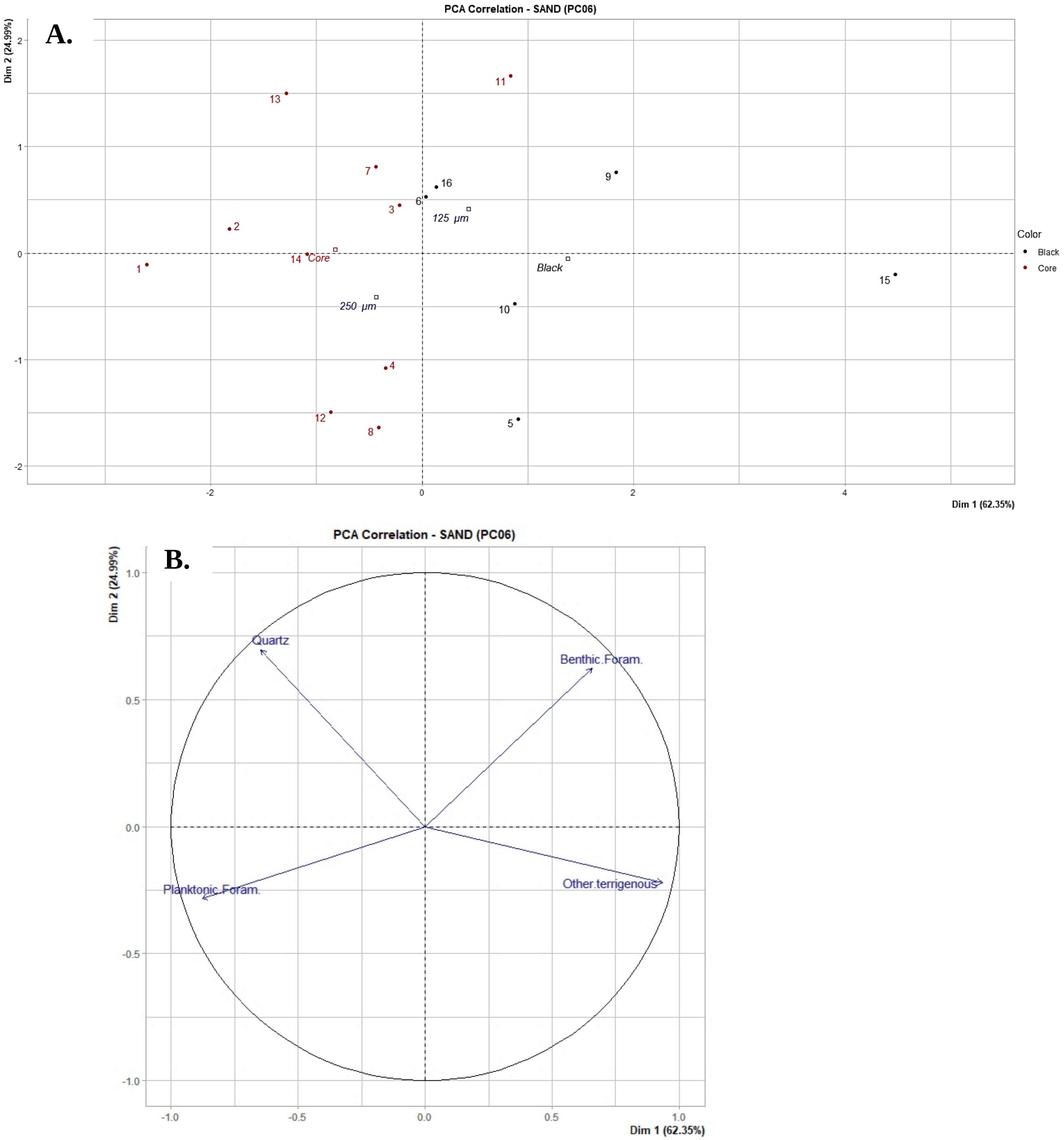

Figure 19. PCA biplots A. with the 16 samples and categorical variables (colour and fractions) and B. simple distribution between the axes PCA 1 and PCA 2, of the composition of the sand from core PC06.

3.3.3 Distribution of smear slide composition

The clustering analysis results (see Figure 20) significantly support the preliminary findings concerning the difference in background sediments and black lenticules composition. Indeed, as seen in Figure 20, nannofossils tend to cluster on the positive side of component 1, whereas pyrite (and organic matter) distribution is oriented to its negative side. The background sediments (numbers 1 in Figure 20) are dominated by clay minerals and nannofossils, whereas the black lenticules (numbers 2 in Figure 20) are dominated by pyrite and organic compounds. The average distance from the centroid (1) in these data (see Appendix I) is lowest for pyrite (0,833) and highest for nannofossils (44,42).

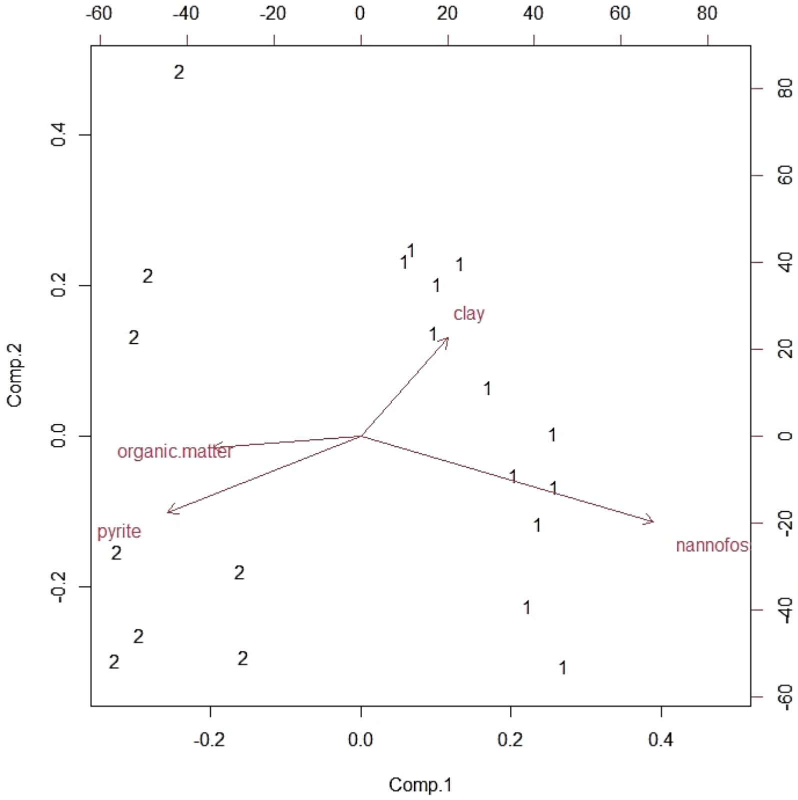

Figure 20. Results of the clustering analysis (k-mean) presented in a biplot. For the analysis, two groups were defined: (1) background sediments and (2) black lenticules, as well as four variables (components): clay, nannofossils, organic matter, and pyrite.

4 DISCUSSION

4.1 Sedimentary-stratigraphic interpretation

Based on texture, mean grain-size, sorting, percentage of carbonates (measured), and component types (terrigenous, biogenic, authigenic, and organic matter), as well as the visual observation (contact and structures), four main lithofacies define sedimentary units making up the stratigraphy of the core, from the bottom to the top: A- Pyritic mud (from 324,5 to 220 cm BSF), B- Pyritic organic-rich mud (from 220 to 132 cm BSF), C- Clay-rich mud (from 132 to 75 cm BSF), and D- Pelagic mud (from 75 to 0 cm BSF).

- From 49 kyrs. BP to 34 kyrs. BP – Sedimentary unit A

It extends from 324,5 up to 244 cm BSF and is dominated by very slightly sandy clayey silt (up to 64% silt) sediments, and the mean grain-size reaches the higher value of the whole core (up to 6,3 μm) before slowly decreases (down to 3 μm). Sediments are very poorly sorted, and carbonates contents are low to moderate (down to 17%) (see Figure 10 and Table 7). Terrigenous components predominate, with clay minerals (around 25-30%) dominating (as seen in Figure 14) and authigenic components (up to 40% pyrite). This unit presents gradual bedding contact and is marked by rare bioturbations (mostly pyritized burrows as seen in Figure 9) but lacks significant trace fossils (such as feeding structures). It is strongly dominated by black lenticules (see Figure 10, U-channels photo).

- From 34 kyrs. BP to 21 yrs. BP – Sedimentary unit B

It extends from 220 up to 132 cm BSF and is mostly composed of clayey silt (up to 57% silt). It is also characterised by a slight increase in mean average grain-size (from 3 to 4.5 μm), with very poorly sorted sediments (see Figure 10 and Table 7). Carbonates contents appear moderate (<30%), and authigenic components (mostly pyrite, as shown in Figure 14) as well as organic materials (both >20%) predominate in this unit. It is interesting to observe an increase in heavy minerals (around 160-150 cm BSF) (see Figure 14). Plus, bioturbation is nearly non-existent, only pyritized burrows (see Figure 9) may be detected in the unit, verifying the pyrite contents (see Figure 14).

- From 21 kyrs. BP to 11,5 kyrs. BP – Sedimentary unit C

It extends from 132 up to 75 cm BSF and is defined by very slightly sandy clayey silt (up to 59% silt), and it has a larger mean average grain-size (5-6 µm). Moreover, carbonates concentration keeps moderate, with a rapid decline until 20%, then gradually increases again (see Figure 10). The unit is dominate by terrigenous components (>30% of clay minerals), as well as organic matter and pyrite (both up to 25%). In addition, this unit has a BI value near 1 (see Figure 9), which corresponds to rare bioturbation with very few discrete traces (see Appendix E), with rare black lenticules.

- From 11,5 yrs. BP to present days – Sedimentary unit D

It extends from 75 up to 0 cm BSF and is mostly made of very slightly sandy silty clay (up to 56% clay) and has an average particle size of 3-4 µm (see Figure 10 and Table 7). This unit has the highest carbonate concentration (up to 40%) and is mostly made of biogenic components (>50%) planktonic foraminifera (see Figure 11) and nannofossils (see Figure 14). Furthermore, the unit has the highest BI (=2) (see Appendix D), which is primarily marked by *Thalassinoides*-like traces (see Figure 9) mostly between 0 and 66 cm BSF. Black lenticules are absent in this unit, only background sediments can be observed.

Table 7. Synthetic table presenting the main characteristics: texture, median–D50, sorting–σ, composition (carbonates–%, and dominant component: terrigenous–T, biogenic–B, authigenic–A, and organic matter–OM), as well as visual observation (contact and structures) for each defined units: A- Pyritic mud (from 324,5 to 220 cm BSF), B- Pyritic organic-rich mud (from 220 to 130 cm BSF), C- Clay-rich mud (from 130 to 75 cm BSF), and D- Pelagic mud (from 75 to 0 cm BSF).

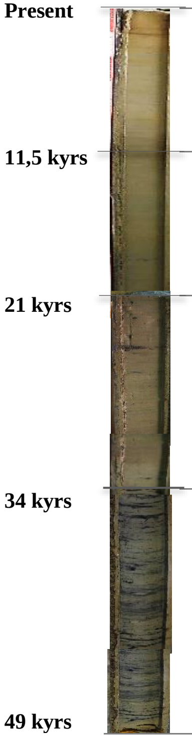

Unit	Interp.	Texture	Mean (µm)	Sorting (σ)	Composition		Visual observation	
					Carbonates (%)	*Dominantly*	*Contacts*	*Structures*
D	Microfossil-rich mud	Very slightly sandy silty clay (up to 56% clay)	3-4 µm	Very poorly sorted	High (up to 40%)	**B**: Planktonic foraminifera (>50%), and nannofossils (>40%)	Gradual	Low bioturbation
C	Clay-rich mud	Very slightly sandy clayey silt (up to 59% silt)	5-6 µm	Very poorly sorted	Moderate (up to 25%)	**T-A**: Clay minerals (>30%), and pyrite (up to 25%), as well as **OM** (up to 25%)	Gradual	Rare bioturbation, rare black lenticules
B	Pyritic organic-rich mud	Clayey silt (up to 57% silt)	From 3 to 4.5 µm	Very poorly sorted	Moderate (<30%)	**OM** (>20%), and **A**: pyrite (>20%)	Gradual	Rare bioturbation, several black lenticules
A	Pyritic mud	Very slightly sandy clayey silt (up to 64% silt)	Up to 6,3 µm	Very poorly sorted	Low to moderate (down to 17%)	**T-B-A**: Clay minerals (25%), nannofossils (30%), and pyrite (up to 40%)	Gradual	Rare bioturbation, dominated by black lenticules

4.2 Interpreting the sedimentary processes

Definition of the processes responsible of the transport and deposition of sediments in deep-water is not an always easy task, mainly for the muddy sediments (i.e., Alonso et al. 2016; Stow 1979; Stow et al. 2002; Stow and Faugères 2008). Differentiation between hemipelagites, fine contourites and fine turbidites is also a matter of debate, because of their close process interaction. This is because the lateral advection that involves the hemipelagic process can be provoked by the slow action of bottom currents action; and, because the very slow deposition from the suspension finer cloud of a turbidity flow can result in a hemiturbidite deposition.

On the southern flank of the Portimão seamount previous studies (i.e., Silva et al. 2020) based on seismic records indicate that downslope processes predominate on the flanks, mainly in the form of mass flow and mass transport deposits. However, the sediment record by PC06 deep-sea core does not show the occurrence of this type of processes and/or potential occurrence of related turbidity flows. The lack of sharp and/or erosive stratigraphic boundaries, levels with textural fining-upward trends, and sudden changes sediment composition pointing to episodic events from different sources, tentatively suggest the lack of fine muddy turbidites. Then, the muddy sediments would represent hemipelagites and/or fine contourites.

The Portimão bank forms a topographic bulge that may affect the circulation of the NADW and create turbulences and faster flows on the sides created by its deflection when it meets the seamount, as it has been typically described in other deep-water seamounts (i.e., Faugères et al. 1999; Ercilla et al. 2011). As PC06 core is located on the southern flank, the bottom current action of that water mass should be also considered as a potential mechanism of sediment transport and deposition.

The units A to C are slightly coarser than unit D, and units A to C show centimetric level alternations with changes in the silt, clay, and sand content. Both observations could be interpreted as variations in the velocity of the transporting bottom current over time at two different temporal scales: i) from the glacial (A to C) to interglacial (D) periods; and ii) as short-scale variations during the A to C unit sedimentation. This scenario point to at least sediments comprising units A to C could be interpreted as fine contourites deposited from suspension loads under relatively weak bottom currents. Significant silt peaks and elevated D50 values, particularly during Heinrich Events (especially HE5 and HE1), in conjunction with the ascending Zr/Al ratios during these intervals, suggest a relatively higher impact of bottom currents (see Figure 21). Nevertheless, more analysis to characterize the stratigraphy of contourite sequences would help to confirm this interpretation.

On the other hand, the predominance of terrigenous particles in units A-C *versus* biogenic in unit D, could reflect the decreases of influence of the inland sediment supply during the Holocene. Likewise, the unit D is predominantly muddier than the underlying units. Both facts point that hemipelagic settling of marine micro skeletons and terrigenous particles sedimentation would be responsible for the deposition of unit C.

4.3 Interpretation of environmental changes

4.3.1 Late Pleistocene

- From 49 kyrs. BP to 34 kyrs. BP – Sedimentary unit A

During this period, sedimentary unit A was deposited, corresponding to the last glacial low stand period of sea level (i.e., Cartapanis et al. 2016; Murray-Wallace 2023). The sediment primarily consisted of a very slightly sandy clayey silt, which is indicative of the prevailing conditions created by bottom currents, probably the North Atlantic Deep Water (NADW)'s flow (i.e., Villanueva and Gutierrez-Mas 1994; Wienberg et al. 2010; Nichols et al. 2020). During this period, climate was cooler than present-day, creating colder sea surface temperature in the ocean. The changes in temperature gradients can lead to changes in ocean circulations (i.e., Cartapanis et al. 2016; Genty and Moreno 2021; Murray-Wallace 2023).

The shifts in sea surface temperatures (and nutrient availability) could have influenced the distribution of marine organisms (i.e., Ferreira et al. 2008; Balestra et al. 2017; Penaud et al. 2022). This hypothesis could be corroborated by the presence of fossil assemblages in core PC06, including high percentages of foraminifera (see Figures 11, 12, and 13), and coccolithophores, as indicated in

Table 6 and Figures 15 and 19. To confirm this interpretation, it will be necessary to further study these micro skeletons to determine the habitats of each species present in the core.

Moreover, the presence of pyrite at the base of PC06, and near Portimão seamount, can be attributed to a combination of geological and environmental factors. Anoxic conditions, prevalent in deep waters (and near seamounts), facilitate the reaction between iron and sulphide ions, resulting in the precipitation of pyrite. In addition, high biological activity in surface water can cause a strong accumulation of organic matter in the seabed, favouring the formation of pyrite in sediments with low oxygen content (i.e., Brüchert et al. 2000). The complex interplay of these factors, coupled with variations in ocean circulation, sedimentation rates, and organic matter content, could have shapes the depositional environment (i.e., Magill et al. 2018).

- <u>From 34 kyrs. BP to 21 yrs. BP – Sedimentary unit B</u>

As sedimentary unit B was deposited, marking the culmination of the last glacial period, the predominant control on the accumulation of organic-rich mud was the continuation of glacial conditions. Throughout this period, sea levels experienced a notable drop, reaching their lowest point during the Last Glacial Maximum (LGM). This substantial sea level regression exposed previously submerged coastal areas, including the Iberian coast, leading to a significant influx of terrigenous sediments transported by gravitational forces into the deep sea (i.e., Genty and Moreno 2021).

Additionally, during colder intervals, such as Heinrich events (HE) (and YD), the presence of cold, nutrient-rich water masses facilitated robust primary productivity (PP) combined with the accumulation of organic matter (OM) on the seafloor, as indicated by Br/Ti and Br peaks in Figure 21, contributing to carbon sequestration (i.e., Itambi et al. 2009 ; Stumpf et al. 2011 ; Meinander et al. 2022 ; Penaud et al. 2022; Vandorpe et al. 2022).

Furthermore, the LGM marks a pivotal juncture in the sedimentary sequences for core PC06, occurring roughly 20,000 years BP. This period coincided with a significant sea level regression to approximately -120 to -130 meters below the current mean sea level (MSL), as documented by Cartapanis et al. (2016) and Murray-Wallace (2023).

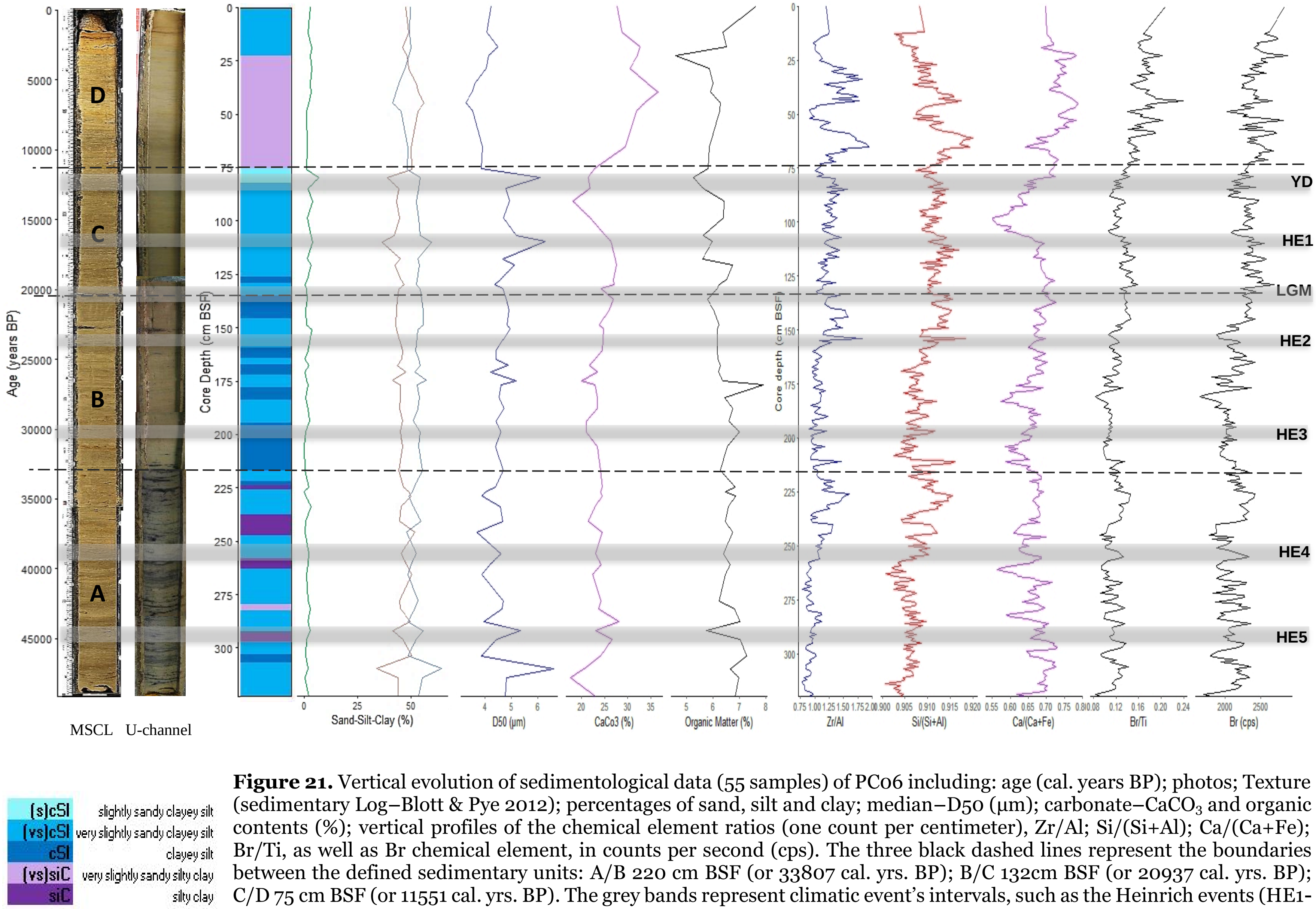

Figure 21. Vertical evolution of sedimentological data (55 samples) of PC06 including: age (cal. years BP); photos; Texture (sedimentary Log–Blott & Pye 2012); percentages of sand, silt and clay; median–D50 (µm); carbonate–$CaCO_3$ and organic contents (%); vertical profiles of the chemical element ratios (one count per centimeter), Zr/Al; Si/(Si+Al); Ca/(Ca+Fe); Br/Ti, as well as Br chemical element, in counts per second (cps). The three black dashed lines represent the boundaries between the defined sedimentary units: A/B 220 cm BSF (or 33807 cal. yrs. BP); B/C 132cm BSF (or 20937 cal. yrs. BP); C/D 75 cm BSF (or 11551 cal. yrs. BP). The grey bands represent climatic event's intervals, such as the Heinrich events (HE1-5), the Last Glacial Maximum (LGM), and the Younger Dryas (YD).

The climate during the LGM was notably colder than present-day conditions, with global temperatures estimated to be several degrees Celsius lower (i.e., Scott-Elias 2007). These climatic changes corresponded to the transition from sedimentary unit C, characterized by pyritic organic-rich mud (see Table 7), to unit B, primarily characterized by clay-rich mud (Table 7). This transition marked the shift from anoxic (poor-oxygen) conditions, evidenced by pyritized burrows (Figure 9) and mineralogical analysis (up to 25% pyrite content in unit C, see Figure 14), to well-oxygenated conditions, as indicated by a Bioturbation Index (BI=1) in Figure 9.

During the LGM, significant alterations occurred in water masses (certainly temperature and salinity), including the Mediterranean Outflow Waters (MOW), the Eastern North Atlantic Central Water (ENACW), and the North Atlantic Deep Waters (NADW) (i.e., García et al. 2020), as supported by the increasing trends in bottom current indicators (see D50 and the Zr/Al ratio in Figure 21). These alterations led to densification, resulting in increased flow velocities, as evidenced by peaks in D50 values during cold periods in Figure 21. This adjustment in water masses dictated the transport distance of clay-sized particles, with some peaks in bottom current (D50) aligning with silt peaks (see Figure 21) (i.e., Voelker et al. 2007; Colmenero-Hidalgo et al. 2004; Stumpf et al. 2011; and García et al. 2020).

- <u>From 21 kyrs. BP to 11,5 kyrs. BP – Sedimentary unit C</u>

The deposition of sedimentary unit C corresponds to the Last Glacial to Interglacial transition, marked a transformative epoch in the Gulf of Cadiz, unveiling dynamic shifts in climate, oceanography, and sedimentation (i.e., Blockley et al. 2012). It corresponds to a post-glacial warming period, during which global temperatures experienced a significant rise, propelling the melting of ice sheets and glaciers and consequent sea level elevation.

The Gulf of Cadiz, situated in the northeastern Atlantic, bore witness to changes in ocean circulation patterns, including potential alterations in the Atlantic Meridional Overturning Circulation (AMOC), impacting heat transport and regional climate dynamics. Concurrently, sea surface temperatures in the Gulf underwent modifications, influencing marine ecosystems and precipitation.

Sedimentation patterns in the region underwent shifts as well, reflecting the interplay of factors such as changing nutrient availability, water temperature, and productivity. The rise in sea levels inundated continental shelves, reshaping the landscape, and influencing the transport and deposition of sediment in the Gulf (i.e., Shepard 1977; Nichols 2009; Blockley et al. 2012).

In mid-latitude environments, the primary mechanism of chemical weathering is hydrolysis, a process highly sensitive to environmental factors, particularly precipitation and temperature. The sensitivity of this process to prevailing climatic conditions carries significant implications for the interpretation of the results, particularly concerning the abundance of sediments dominated by clay, as depicted in Figure 20. These clay-rich sediments are most prominently associated with unit C, as visually represented in Figure 21.

Furthermore, the deposition of these clay-rich sediments, as detailed in Table 7, is influenced by additional factors such as coastal exposure and sediment transport via gravity processes. This underscores the pivotal role of sea level fluctuations in the study area (i.e., Gràcia et al. 2010; Cartapanis et al. 2016; Murray-Wallace 2023). These combined factors contribute to the distinctive sedimentary characteristics observed in unit.

4.3.2 Holocene

- From 11,5 yrs. BP to present days – Sedimentary unit D

During the deposition of sedimentary unit D, relatively stable and warm climatic conditions were established. This period followed the deglaciation, occurring approximately 11,700 years BP, marking the end of the Younger Dryas (YD) period. During this transition, sea level underwent a rapid and substantial rise (i.e., Cartapanis et al. 2016; Murray-Wallace 2023). This sea level rise and increased temperatures, estimated at approximately 75 cm below sea floor (BSF), coinciding with the predominance of (hemi)pelagic sedimentation characteristics in unit D. This sedimentary unit is rich in planktonic foraminifera and nannofossils (see Table 7).

The warm climatic conditions are further reflected in the increased concentrations of calcium carbonate (CaCO3), reaching up to 40%, and a rise in paleoproductivity, as indicated by the Ca/(Ca/Fe) ratio in Figure 21. Most of the trace fossils observed in this deposit correspond to feeding structures, which are common in (hemi)pelagic environments, characterized by low-energy and stable habitats (i.e., Dorador and Rodríguez-Tovar 2014; Gingras et al. 2014).

Notably, core PC06 exhibits a significant abundance of coccolithophorids, one of the most prominent phytoplankton groups with a substantial role in marine primary productivity (PP) (i.e., Colmenero-Hidalgo et al. 2004; Ferreira et al. 2008; Balestra et al. 2017).

During the Holocene, characterized by relatively warmer ocean temperatures and increased insolation in the photic zone, conditions favoured the presence of high levels of calcium carbonates (CaCO3), reaching up to 40%, and elevated levels of (Ca/(Ca+Fe)). These favourable conditions are indicated by the presence of bioturbations, such as feeding structures, as seen in Figure 9. These environmental changes could be influenced by potential atmospheric fertilization, attributed to the proximity of the Gulf of Cadiz to the Sahara. This interpretation can be suggested based on the peaks in Si/(Si+Al) ratios, observed in Figure 21 during dry periods (i.e., Rodrigo-Gámiz et al. 2011), nevertheless further studies are needed to confirm this hypothesis.

4.4 Paleoceanographic conditions and pyrite formation during the Late Pleistocene

During the time span from 49,171 years BP to 20,937 years BP, sediment deposits in the studied area exhibited a notable abundance of pyrite and organic matter. Deep-sea sediments, particularly in the lower sections, reveal distinctive features, illustrated by the identification of black lenticules in the last two sedimentary units of the PC06 core, as shown in the U-channel photo. This observation likely indicates a significant decrease in oxygen levels in sedimentary layers. The prevalence of these black lenticules provides valuable insight into persistent low-oxygen conditions in the deep-sea environment, particularly in the lower strata of the examined core. This low-oxygen condition was further illustrated by the low bioturbation index observed in these units, as depicted in Figure 9. As previously mentioned, during colder periods, there is an upsurge in PP in the upper ocean layers. Cold, nutrient-rich waters act as a catalyst for the flourishing growth of phytoplankton, which subsequently descends to the ocean depths and accumulates on the seafloor (i.e., Brüchert et al. 2000; Eynaud et al. 2009; Fink et al. 2013; Balestra et al. al. 2017; Penaud et al. 2022). This accumulation leads to a substantial production of OM that undergoes decomposition. During this process, sulphur compounds are generated and have the potential to react with iron minerals, ultimately culminating in the formation of pyrite (i.e., Chester and Jickells 2012; Magill et al. 2018; Wade et al. 2020).

It's important to note that the quantity of pyrite that could develop in a deposit, as observed in core PC06 (see Table 6, Figures 10, and 14), depended on the supply rates of decomposable organic matter, dissolved sulphate, and reactive detrital iron minerals (i.e., Chester and Jickells 2012; Magill et al. 2018; Wade et al. 2020).

These oxygen-reducing conditions were pivotal for pyrite formation and encompassed the following key processes, as delineated by Chester and Jickells (2012):

1) Decomposition of organic matter (as expressed in Equation 1): This chemical reaction resulted in the breakdown of organic matter (CH_2O), yielding hydrogen sulphide (H_2S) and carbon dioxide (CO_2) while consuming the OM.
2) Generation of hydrogen sulphide (as depicted in Equation 2).
3) Pyrite precipitation (as demonstrated in Equation 3): During this phase, iron disulfide (pyrite) materialized, precipitating from pore waters and sediments, ultimately forming pyrite minerals within the sediments.

$$2CH_2O + SO4^{2-} \rightarrow 2CO_2 + H_2S + H_2O \qquad \text{(Equation 1.)}$$

$$Fe(OH)_3 + H_2S \rightarrow FeS + 3H_2O \qquad \text{(Equation 2.)}$$

$$2FeS + H_2S \rightarrow FeS_2 + H_2O \qquad \text{(Equation 3.)}$$

Furthermore, the composition of the black lenticules can suggested an intimate link between the accumulation of organic carbon and intensity of upwelling, as demonstrated by Brüchert et al. (2000) for the Benguela systems. The abrupt transition from nannofossils-rich sediments above pyritic organic-rich sediments may reflect a sudden change in paleo circulation patterns (shifts in temperature gradient), which could have caused a seaward shift of the upwelling surface (i.e., Brüchert et al. 2000; Rogerson et al. 2004; Eynaud et al. 2009; Murray-Wallace 2023).

5 CONCLUSIONS

In the present work, we aimed to reconstruct the paleoenvironmental conditions as documented in core PC06, recovered from the base of the Portimão Bank in the southwestern Gulf of Cadiz. This multidisciplinary study of the core provides a comprehensive overview of paleoenvironmental changes in the study area, both general and local in nature.

The sedimentary-stratigraphic interpretation of the PC06 core provides valuable information on environmental changes that occurred during the Late Pleistocene and Holocene epochs. Four main lithofacies (pyritic mud, organic-rich pyritic mud, clay-rich mud, and pelagic mud) define sedimentary units, each reflecting specific conditions and processes.

During the period from 49,000 years before present (BP) to 34,000 years BP (sedimentary unit A), sediment deposition in the Gulf of Cadiz occurred during the last period of glacial low settlement. The sedimentary composition, characterized by very slightly sandy clayey silts, suggests the influence of bottom currents, potentially associated with the flow of deep waters from the North Atlantic. The predominance of pyrite and fossil assemblages indicates the impact of anoxic conditions and variations in ocean circulation on the depositional environment.

From 34,000 years BP to 21,000 years BP (sedimentary unit B), the peak of the last ice age witnessed the deposition of organic-rich muds. Sea level regression has exposed coastal areas, leading to an influx of terrigenous sediments. Cold intervals, characterized by Heinrich Events, facilitated primary productivity and accumulation of organic matter. The shift from anoxic to well-oxygenated conditions during the Last Glacial Maximum significantly influenced sediment characteristics.

During the later period from 21,000 years BP to 11,500 years BP (sedimentary unit C), the transition from the last glacial to the interglacial period influenced sedimentation patterns. Changes in ocean circulation, sea surface temperatures, and sea level rise have played a central role, contributing to the characteristics of clay-rich sediments. Environmental changes, including increasing global temperatures and rising sea levels, have had significant consequences on sediment transport and deposition.

From 11,500 years BP to the present (sedimentary unit D), the Holocene experienced stable and warm climatic conditions. The interaction of sea level rise and increasing temperatures influenced sedimentation, leading to the predominance of (hemi)pelagic features. The presence of planktonic foraminifera, nannofossils and coccolithophores indicates favourable conditions for marine life. The deposition of calcium carbonate-rich sediments reflects a shift toward more stable and productive environments.

The interpretation of sedimentary processes unveils the complexity of deep-water transport and deposition, encompassing considerations for hemipelagites, fine contourites, and fine turbidites. The influence of the Portimão Bank on bottom currents and sedimentation patterns is highlighted, with core PC06 lacking mass flow and mass transport deposits.

The paleoceanographic conditions during the late Pleistocene highlight the complex interaction of climate, sea level changes, and ocean circulation. Key periods such as the Last Glacial Maximum, the Heinrich events, and the transition to the Holocene demonstrate the sensitivity of sedimentary responses to environmental changes. The presence of pyrite and organic matter in sediments is attributed to anoxic conditions, microbial processes, and changes in paleo circulation patterns.

In conclusion, the comprehensive analysis of sedimentary units, processes and paleoceanographic conditions provides a nuanced understanding of the environmental evolution of the Portimão Bank over the last 49,000 years.

However, it is crucial to recognize the limitations inherent in this study. Many unresolved questions persist, highlighting the need for further research to deepen our understanding of sedimentary processes in the Gulf of Cadiz, particularly in areas such as the Portimão Bank. Our research highlighted significant knowledge gaps related to factors contributing to anoxic conditions in the region. The complex interaction between tectonic activity, a known influencing factor in this region, and sedimentary patterns requires further exploration. Additionally, a careful reassessment of the classification of these deposits as (hemi)pelagic and contourites is essential for accurate categorization. Additionally, advancing our understanding of this unique marine environment requires significant improvement in data resolution. These proposed avenues of research highlight the inherent complexity of the Gulf of Cadiz and highlight the central role of sustained scientific exploration to obtain comprehensive information on environmental transformations in this region.

Bibliography

Alonso B, Ercilla G, Casas D, Stow V, Rodríguez-Tovar FJ, Dorador J, Francisco Javier Hernandéz-Molina. 2016. Contourite vs gravity-flow deposits of the Pleistocene Faro Drift (Gulf of Cadiz): Sedimentological and mineralogical approaches. Marine Geology, 377, 77-94. 377:77–94. doi:https://doi.org/10.1016/j.margeo.2015.12.016.

Bahr A, Jiménez-Espejo FJ, Kolasinac N, Grunert P, Hernández-Molina FJ, Röhl U, Voelker AHL, Escutia C, Stow DAV, Hodell D, et al. 2014. Deciphering bottom current velocity and paleoclimate signals from contourite deposits in the Gulf of Cadiz during the last 140 kyr: An inorganic geochemical approach. Geochemistry, Geophysics, Geosystems. 15(8):3145–3160. doi:https://doi.org/10.1002/2014gc005356.

Balestra B, Grunert P, Ausin B, Hodell D, Flores J-A, Alvarez-Zarikian CA, Hernandez-Molina FJ, Stow D, Piller WE, Paytan A. 2017. Coccolithophore and benthic foraminifera distribution patterns in the Gulf of Cadiz and Western Iberian Margin during Integrated Ocean Drilling Program (IODP) Expedition 339. Journal of Marine Systems. 170:50–67. doi:https://doi.org/10.1016/j.jmarsys.2017.01.005.

Bard E, Rostek F, Guillemette Ménot-Combes. 2004. Radiocarbon calibration beyond 20,000 ^{14}C yr B.P. by means of planktonic foraminifera of the Iberian Margin. Quaternary Research. 61(2):204–214. doi:https://doi.org/10.1016/j.yqres.2003.11.006.

Blaauw M. 2010. Methods and code for “classical” age-modelling of radiocarbon sequences. Quaternary Geochronology. 5(5):512–518. doi:https://doi.org/10.1016/j.quageo.2010.01.002.

Blockley SPE, Lane CS, Hardiman M, Rasmussen SO, Seierstad IK, Steffensen JP, Svensson A, Lotter AF, Turney CSM, Bronk Ramsey C. 2012. Synchronisation of paleoenvironmental records over the last 60,000 years, and an extended INTIMATE event stratigraphy to 48,000 b2k. Quaternary Science Reviews. 36:2–10. doi:https://doi.org/10.1016/j.quascirev.2011.09.017.

Blott SJ, Pye K. 2001. GRADISTAT: a grain-size distribution and statistics package for the analysis of unconsolidated sediments. Earth Surface Processes and Landforms. 26(11):1237–1248. doi:https://doi.org/10.1002/esp.261.

Brüchert V, Pérez MElena, Lange CB. 2000. Coupled primary production, benthic foraminiferal assemblage, and sulfur diagenesis in organic-rich sediments of the Benguela upwelling system. Marine Geology. 163(1-4):27–40. doi:https://doi.org/10.1016/s0025-3227(99)00099-7.

Burton EA. 1998. Carbonate compensation depth. In: Geochemistry. Encyclopedia of Earth Science. Marshall CP, Fairbridge RW, editors. https://doi.org/10.1007/1-4020-4496-8_46.

Cartapanis O, Bianchi D, Jaccard SL, Galbraith ED. 2016. Global pulses of organic carbon burial in deep-sea sediments during glacial maxima. Nature Communications. 7(1). doi:https://doi.org/10.1038/ncomms10796.

Chester R, Jickells T. 2012. Marine Geochemistry. Wiley-Blackwell. doi:10.1002/9781118349083.

Cochran JK, Bokuniewicz HJ, Yager PL. 2019. Encyclopedia of Ocean Sciences . https://www.sciencedirect.com/referencework/9780128130827/encyclopedia-of-ocean-sciences.

Colmenero-Hidalgo E, Flores J-A, Sierro FJ, Bárcena MÁngeles, Löwemark L, Schönfeld J, Grimalt JO. 2004. Ocean surface water response to short-term climate changes revealed by coccolithophores from the Gulf of Cadiz (NE Atlantic) and Alboran Sea (W Mediterranean). Palaeogeography, Palaeoclimatology, Palaeoecology. 205(3-4):317–336. doi:https://doi.org/10.1016/j.palaeo.2003.12.014.

Dansgaard W, Johnsen SJ, Clausen HB, Dahl-Jensen D, Gundestrup NS, Gundestrup CU, Steffensen JP. 1993. Evidence for general instability of past climate from a 250-kyr ice-core record. doi:10.1038/364218a0.

Dorador J, Rodríguez-Tovar FJ. 2013. Digital image treatment applied to ichnological analysis of marine core sediments. Iodp Expedition Scientists, editor. Facies. 60(1):39–44. doi:https://doi.org/10.1007/s10347-013-0383-z.

Dorador J, Rodríguez-Tovar FJ. 2014. A Novel Application of Digital Image Treatment By Quantitative Pixel Analysis To Trace Fossil Research In Marine Cores. PALAIOS. 29(10):533–538. doi:https://doi.org/10.2110/palo.2014.044.

Ercilla G, Casas D, Vázquez JT, Iglesias J, Somoza L, Juan C, ERGAP Project and Cruise Teams. 2011. Imaging the recent sediment dynamics of the Galicia Bank region (Atlantic, NW Iberian Peninsula). Marine Geophysical Research, 32, 99-126. doi:10.1007/s11001-011-9129-x.

Eynaud F, de Abreu L, Voelker A, Schönfeld J, Salgueiro E, Turon J-L, Penaud A, Toucanne S, Naughton F, Sánchez Goñi MF, et al. 2009. Position of the Polar Front along the western Iberian margin during key cold episodes of the last 45 ka. Geochemistry, Geophysics, Geosystems. 10(7):n/a-n/a. doi:https://doi.org/10.1029/2009gc002398.

Faugères J-C, Stow DAV, Imbert P, Viana A. 1999. Seismic features diagnostic of contourite drifts. Marine Geology. 162(1):1–38. doi:https://doi.org/10.1016/s0025-3227(99)00068-7.

Fernández-Puga MC, Vázquez JT, Roque C, Alonso B, Medialdea Cela T, Palomino D, Ercilla G, Díaz del Río V, Somoza L. 2014. Morphological features of the Portimao Bank Seamount (NW Gulf of Cadiz Margin) related to Pliocene-Quaternary activity. digitalcsices. https://digital.csic.es/handle/10261/116775.

Ferreira J, Cachão M, González R. 2008. Reworked calcareous nannofossils as ocean dynamic tracers: The Guadiana shelf case study (SW Iberia). Estuarine, Coastal and Shelf Science. 79(1):59–70. doi:https://doi.org/10.1016/j.ecss.2008.03.012.

Fink HG, Wienberg C, De Pol-Holz R, Wintersteller P, Hebbeln D. 2013. Cold-water coral growth in the Alboran Sea related to high productivity during the Late Pleistocene and Holocene. Marine Geology. 339:71–82. doi:https://doi.org/10.1016/j.margeo.2013.04.009.

García M, Llave E, Hernández-Molina FJ, Lobo FJ, Ercilla G, Alonso B, Casas D, Mena A, Fernández-Salas LM. 2020. The role of late Quaternary tectonic activity and sea-level changes on sedimentary processes interaction in the Gulf of Cadiz upper and middle continental slope (SW Iberia). Marine and

Petroleum Geology. 121:104595. doi:https://doi.org/10.1016/j.marpetgeo.2020.104595. https://www.sciencedirect.com/science/article/abs/pii/S0264817220303780.

Genty D, Moreno A. 2021. Paleoclimatology. Ramstein G, Landais A, Bouttes N, Sepulchre P, Govin A, editors. Springer.

Gingras MK, Pemberton SG, Smith M. 2014. Bioturbation : Reworking Sediments for Better or Worse. Schlumberger, editor. https://wwwresearchgatenet Oilfield Review 46(6):46-58. https://www.researchgate.net/publication/287329471_Bioturbation_Reworking_sediments_for_better_or_worse.

Gràcia E, Vizcaino A, Escutia C, Asioli A, Rodés Á, Pallàs R, Garcia-Orellana J, Lebreiro S, Goldfinger C. 2010. Holocene earthquake record offshore Portugal (SW Iberia): testing turbidite paleoseismology in a slow-convergence margin. Quaternary Science Reviews. 29(9-10):1156–1172. doi:https://doi.org/10.1016/j.quascirev.2010.01.010.

Habgood EL, Kenyon NH, Masson DG, Akhmetzhanov A, Weaver PPE, Gardner J, Mulder T. 2003. Deep-water sediment wave fields, bottom current sand channels and gravity flow channel-lobe systems: Gulf of Cadiz, NE Atlantic. Sedimentology. 50(3):483–510. doi:https://doi.org/10.1046/j.1365-3091.2003.00561.x.

Hernandéz-Molina FJ, Serra N, Stow V, Llave E, Ercilla G, Van Rooij D. 2011. Along-slope oceanographic processes and sedimentary products around the Iberian margin. Geo-marine Letters. 31(5-6):315–341. doi:https://doi.org/10.1007/s00367-011-0242-2.

Hesse R, Schacht U. 2011. Developments in Sedimentology - Chapter 9 - Early Diagenesis of Deep-Sea Sediments. HüNeke H, Mulder T, editors. ScienceDirect. 63:557–713. https://www.sciencedirect.com/science/article/abs/pii/B9780444530004000093.

Hillaire-Marcel C, De Vernal A. 2007. Proxies in late cenozoic paleoceanography. Amsterdam ; London: Elsevier.

Voelker A, de Abreu L, Abrantes F. 2007. Winter mixed layer conditions in the mid-latitude North Atlantic during MIS 11. http://hdl.handle.net/10400.9/3020.

Hüneke H, Henrich R. 2011. Developments in Sedimentology - Chapter 4 - Pelagic Sedimentation in Modern and Ancient Oceans. HüNeke H, Mulder T, editors. ScienceDirect. 63:215–351. https://www.sciencedirect.com/science/article/abs/pii/B9780444530004000044.

Itambi AC, von Dobeneck T, Mulitza S, Bickert T, Heslop D. 2009. Millennial-scale northwest African droughts related to Heinrich events and Dansgaard-Oeschger cycles: Evidence in marine sediments from offshore Senegal. Paleoceanography. 24(1):n/a-n/a. doi:https://doi.org/10.1029/2007pa001570.

Lagabrielle Y, Maury R, Renard M. 2013. Mémo visuel de géologie. Dunod.

Leckie RM, Tentori D, Doran L. 2015. ODP Smear Slide Digital Reference for Sediment Analysis of Marine Mud. Part 2: Methodology and Atlas of Biogenic Components. http://wwwiodptamuedu/publications/TNhtml. https://doi.org/10.14379/iodp.tn.2.2015.

Llave E, Schönfeld J, Hernández-Molina FJ, Mulder T, Somoza L, Díaz del Río V, Sánchez-Almazo I. 2006. High-resolution stratigraphy of the Mediterranean outflow contourite system in the Gulf of Cadiz during the late Pleistocene: The impact of Heinrich events. Marine Geology. 227(3-4):241–262. doi:https://doi.org/10.1016/j.margeo.2005.11.015.

Lobo FJ, Hernández-Molina FJ, Somoza L, Díaz del RíoV. 2001. The sedimentary record of the post-glacial transgression on the Gulf of Cadiz continental shelf (Southwest Spain). Marine Geology. 178(1-4):171–195. doi:https://doi.org/10.1016/s0025-3227(01)00176-1.

López-González N, Alonso B, Ercilla G, Juan C, Estrada F, García M. 2013. Sediment availability and bottom current intensity vs climatic conditions: the case of the Djibouti contourite system (Alboran Sea, SW Mediterranean). Conference abstracts volume: T3S4_P21. 30th IAS Meeting of Sedimentology, 2-5 September 2013, Manchester. http://hdl.handle.net/10261/89866.

Magill CR, Ausín B, Wenk P, McIntyre C, Skinner L, Martínez-García A, Hodell DA, Haug GH, Kenney W, Eglinton TI. 2018. Transient hydrodynamic effects influence organic carbon signatures in marine sediments. Nature Communications. 9(1):4690. doi:https://doi.org/10.1038/s41467-018-06973-w. https://www.nature.com/articles/s41467-018-06973-w.

Marchès E, Mulder T, Cremer M, Bonnel C, Hanquiez V, Gonthier E, Lecroart P. 2007. Contourite drift construction influenced by capture of Mediterranean Outflow Water deep-sea current by the Portimão submarine canyon (Gulf of Cadiz, South Portugal). Marine Geology. 242(4):247–260. doi:https://doi.org/10.1016/j.margeo.2007.03.013. https://www.sciencedirect.com/science/article/pii/S0025322707000709.

Marsaglia K, Milliken K, Doran L. 2013. IODP Technical Note 1. IODP Digital Reference for Smear Slide Analysis of Marine Mud. Part 1: Methodology and Atlas of Siliciclastic and Volcanogenic Component. http://wwwiodptamuedu/publications/TNhtml. http://dx.doi.org/10.2204/iodp.tn.1.2013.

Martorelli E, Bosman A, Casalbore D, Chiocci F, Conte AM, Di Bella L, Ercilla G, Falcini F, Falco P, Frezza V, et al. 2021. Mid-to-late Holocene upper slope contourite deposits off Capo Vaticano (Mediterranean Sea): High-resolution record of contourite cyclicity, bottom current variability and sandy facies. Marine Geology. 431:106372. doi:https://doi.org/10.1016/j.margeo.2020.106372.

Meinander O, Dagsson-Waldhauserova P, Amosov P, Aseyeva E, Atkins C, Baklanov A, Baldo C, Barr SL, Barzycka B, Benning LG, et al. 2022. Newly identified climatically and environmentally significant high-latitude dust sources. Atmospheric Chemistry and Physics. 22(17):11889–11930. doi:https://doi.org/10.5194/acp-22-11889-2022.

Mestdagh T, Lobo FJ, Llave E, Hernández-Molina FJ, Van Rooij D. 2019. Review of the late Quaternary stratigraphy of the northern Gulf of Cadiz continental margin: New insights into controlling factors and global implications. Earth-Science Reviews. 198:102944. doi:https://doi.org/10.1016/j.earscirev.2019.102944.

Moreno A, Cacho I, Canals M, Grimalt JO, Sánchez-Goñi MF, Shackleton N, Sierro FJ. 2005. Links between marine and atmospheric processes oscillating on a millennial time-scale. A multi-proxy study of the last 50,000yr from the Alboran Sea (Western Mediterranean Sea). Quaternary Science Reviews. 24(14-15):1623–1636. doi:https://doi.org/10.1016/j.quascirev.2004.06.018.

Mulder T, Pascal Lecroart, Hanquiez V, Elodie Marchès, Gonthier E, Guedes J-C, Emmanuelle Thiébot, B. Jaaidi, Kenyon NH, M. Voisset, et al. 2006. The western part of the Gulf of Cadiz: contour currents and turbidity currents interactions. Geo-marine Letters. 26(1):31–41. doi:https://doi.org/10.1007/s00367-005-0013-z.

Murray-Wallace CV. 2023. Barystatic sea-level Changes—glacial–interglacial Cycles☆. ScienceDirect. https://www.sciencedirect.com/science/article/abs/pii/B9780323999311000490.

Nichols G. 2009. Sedimentology and stratigraphy. 2nd ed. Chichester, Uk: Wiley-Blackwell.

Nichols MD, Xuan C, Crowhurst S, Hodell DA, Richter C, Acton GD, Wilson PA. 2020. Climate-Induced Variability in Mediterranean Outflow to the North Atlantic Ocean During the Late Pleistocene. Paleoceanography and Paleoclimatology. 35(9). doi:https://doi.org/10.1029/2020pa003947.

Paulmier A, Ruiz-Pino D. 2009. Oxygen minimum zones (OMZs) in the modern ocean. Progress in Oceanography. 80(3-4):113–128. doi:https://doi.org/10.1016/j.pocean.2008.08.001. https://www.sciencedirect.com/science/article/abs/pii/S0079661108001468.

Penaud A, Eynaud F, Etourneau J, Bonnin J, Vernal A, Zaragosi S, Kim J -H., Kang S, Gal J -K., Oliveira D, et al. 2022. Ocean Productivity in the Gulf of Cadiz Over the Last 50 kyr. Paleoceanography and Paleoclimatology. 37(2). doi:https://doi.org/10.1029/2021pa004316.

Rajput S, Thakur NK. 2016. Geological Controls for Gas Hydrates and Unconventional - Chapter 3 - Sedimentation Pattern. Rajput S, Thakur NK, editors. ScienceDirect.:69–106. https://www.sciencedirect.com/science/article/pii/B9780128020203000035.

Rebesco M, Hernández-Molina FJ, Van Rooij D, Wåhlin A. 2014. Contourites and associated sediments controlled by deep-water circulation processes: State-of-the-art and future considerations. Marine Geology. 352:111–154. doi:https://doi.org/10.1016/j.margeo.2014.03.011.

Reimer PJ, Bard E, Bayliss A, Beck JW, Blackwell PG, Ramsey CB, Brown DM, Buck CE, Edwards RL, Friedrich M, et al. 2013. Selection and Treatment of Data for Radiocarbon Calibration: An Update to the International Calibration (IntCal) Criteria. Radiocarbon. 55(4):1923–1945. doi:https://doi.org/10.2458/azu_js_rc.55.16955.

Relvas P, Barton ED, Dubert J, Oliveira PB, Peliz Á, da Silva JCB, Santos AMP. 2007. Physical oceanography of the western Iberia ecosystem: Latest views and challenges. Progress in Oceanography. 74(2-3):149–173. doi:https://doi.org/10.1016/j.pocean.2007.04.021.

Rodrigo-Gámiz M, Martínez-Ruiz F, Jiménez-Espejo FJ, Gallego-Torres D, Nieto-Moreno V, Romero O, Ariztegui D. 2011. Impact of climate variability in the western Mediterranean during the last 20,000 years: oceanic and atmospheric responses. Quaternary Science Reviews. 30(15):2018–2034. doi:https://doi.org/10.1016/j.quascirev.2011.05.011.
https://www.sciencedirect.com/science/article/abs/pii/S027737911100148X.

Rogerson M, Rohling EJ, Weaver PPE, Murray JW. 2004. The Azores Front since the Last Glacial Maximum. Earth and Planetary Science Letters. 222(3-4):779–789. doi:https://doi.org/10.1016/j.epsl.2004.03.039.

Roque C, Hernández-Molina FJ, Lobo F, Somoza L, Díaz-del-Rio V, Vázquez JT, Dias J. 2010. Geomorphology of the Eastern Algarve proximal continental margin (South Portugal, SW Iberia Peninsula): sedimentary dynamics and its relationship with the last asymmetrical eustatic cycle. Ciências da Terra / Earth Sciences Journal. 17. https://cienciasdaterra.novaidfct.pt/index.php/ct-esj/article/view/263.

Roque C, Silva P, Drago T, Lopes A, Alonso B, Vázquez JT, Casas D, López-González N, Ercilla G, Neres M. 2016. Vertical zonation of bioturbation and mass movements in the Portimão Bank (Gulf of Cadiz, SW Iberia). Csices. doi:http://hdl.handle.net/10261/131384. https://digital.csic.es/handle/10261/131384.

Rothwell RG, Croudace I w. 2015. Twenty Years of XRF Core Scanning Marine Sediments: What Do Geochemical Proxies Tell Us? Micro-XRF Studies of Sediment Cores.:25–102. doi:https://doi.org/10.1007/978-94-017-9849-5_2.

Salgueiro E, Naughton F, Voelker AHL, de Abreu L, Alberto A, Rossignol L, Duprat J, Magalhães VH, Vaqueiro S, Turon J-L ., et al. 2014. Past circulation along the western Iberian margin: a time slice vision from the Last Glacial to the Holocene. Quaternary Science Reviews. 106:316–329. doi:https://doi.org/10.1016/j.quascirev.2014.09.001.

Scott-Elias A, editor. 2007. Encyclopedia of Quaternary Science. ScienceDirect. https://www.sciencedirect.com/referencework/9780444527479/encyclopedia-of-quaternary-science.

Shepard FP. 1977. Geological oceanography: Evolution of coasts, continental margins, and the deep-sea floor. Heinemann London.

Siani G. 2001. Mediterranean Sea Surface Radiocarbon Reservoir Age Changes Since the Last Glacial Maximum. Science. 294(5548):1917–1920. doi:https://doi.org/10.1126/science.1063649.

Silva PF, Roque C, Drago T, Belén A, Henry B, Gemma E, Lopes A, López-González N, Casas D, Naughton F, et al. 2020. Multidisciplinary characterization of Quaternary mass movement deposits in the Portimão Bank (Gulf of Cadiz, SW Iberia). Marine Geology. 420:106086. doi:https://doi.org/10.1016/j.margeo.2019.106086.

Stern JV, Lisiecki LE. 2013. North Atlantic circulation and reservoir age changes over the past 41,000 years. Geophysical Research Letters. 40(14):3693–3697. doi:https://doi.org/10.1002/grl.50679.

Stow D. 1979. Distinguishing between fine-grained turbidites and contourites on the Nova Scotian deep water margin. Sedimentology. 26(3):371–387. doi:https://doi.org/10.1111/j.1365-3091.1979.tb00915.x.

Stow D, Faugères J-C., Gonthier E, Cremer M, Llave E, Hernandez-Molina FJ, Somoza L, Diaz-del-Rio V, Stow D, Faugeres J-C ., et al. 2002. Faro-Albufeira drift complex, northern Gulf of Cadiz - In: Deep-Water Contourite Systems: Modern Drifts and Ancient Series, Seismic and Sedimentary Characteristics. Geol. Soc. Lond. Mem. 22(1), pp. 137–154. Stow DAV, Pudsey CJ, Howe JA, Faugeres J-C ., Viana AR, editors. eprintssotonacuk.:137–154. https://eprints.soton.ac.uk/16317/.

Stow D, Faugères J-C. 2008. Chapter 13 Contourite Facies and the Facies Model - In: Contourites, Development in Sedimentology. Elsevier, Amsterdam, pp. 223–256. Rebesco M, Camerlenghi A, editors. ScienceDirect. 60:223–256. https://www.sciencedirect.com/science/article/abs/pii/S0070457108100139.

Stow D, Smillie Z, Esentia IP. 2018. Deep-sea bottom currents: Their nature and distribution. In Encyclopedia of ocean sciences: earth systems and environmental sciences. Springer.

Stumpf R, Frank M, Schönfeld J, Haley BA. 2011. Climatically driven changes in sediment supply on the SW Iberian shelf since the Last Glacial Maximum. Earth and Planetary Science Letters. 312(1-2):80–90. doi:https://doi.org/10.1016/j.epsl.2011.10.002.

Talley LD, Pickard GL, Emery WJ, Swift JH. 2011. Descriptive Physical Oceanography - Chapter 9 - Atlantic Ocean. Talley LD, Pickard GL, Emery WJ, Swift JH, editors. ScienceDirect.:245–301. https://www.sciencedirect.com/science/article/abs/pii/B9780750645522100095.

Terrinha P, Matias L, Vicente J, Duarte J, Luís J, Pinheiro L, Lourenço N, Diez S, Rosas F, Magalhães V, et al. 2009. Morphotectonics and strain partitioning at the Iberia–Africa plate boundary from multibeam and seismic reflection data. Marine Geology. 267(3-4):156–174. doi:https://doi.org/10.1016/j.margeo.2009.09.012.

Vandorpe T, Delivet S, Blamart D, Wienberg C, Bassinot F, Mienis F, Stuut JW, Van Rooij D. 2022. Palaeoceanographic and hydrodynamic variability for the last 47 kyr in the southern Gulf of Cadiz (Atlantic Moroccan margin): Sedimentary and climatic implications. The Depositional Record. doi:https://doi.org/10.1002/dep2.212.

Vázquez JT, Alonso B. 2012. INFORME CIENTÍFICO – TÉCNICO. Campaña MONTERA-0412. wwwrepositorioieoes. [accessed 2022 Dec 9]. http://www.repositorio.ieo.es/e-ieo/handle/10508/994?locale-attribute=en.

Vázquez JT, Alonso B, Fernández-Puga MC, Gómez-Ballesteros M, Iglesias J, Palomino D, Roque C, Ercilla G, Díaz-del-Río V. 2015. Seamounts along the Iberian Continental Margins. Boletín Geológico y Minero. 126(2-3):483–514.

Villanueva P, Gutierrez-Mas J. 1994. THE HYDRODYNAMICS OF THE GULF OF CÀDIZ AND THE EXCHANGE OF WATER MASSES THROUGH THE GIBRALTAR STRAIT. International Hydrographic Review. 1(1). https://journals.lib.unb.ca/index.php/ihr/article/download/23217/26992.

Wade BS, O'Neill JF, Phujareanchaiwon C, Ali I, Lyle M, Witkowski J. 2020. Evolution of deep-sea sediments across the Paleocene-Eocene and Eocene-Oligocene boundaries. Earth-Science Reviews. 211:103403. doi:https://doi.org/10.1016/j.earscirev.2020.103403.

Waelbroeck C, Duplessy J-C, Michel E, Labeyrie L, Paillard D, Duprat J. 2001. The timing of the last deglaciation in North Atlantic climate records. Nature. 412(6848):724–727. doi:https://doi.org/10.1038/35089060.

Wienberg C, Frank N, Kenneth Neil Mertens, Stuut J-BW, Marchant M, Fietzke J, Furu Mienis, Dierk Hebbeln. 2010. Glacial cold-water coral growth in the Gulf of Cadiz: Implications of increased palaeo-productivity. Earth and Planetary Science Letters. 298(3-4):405–416. doi:https://doi.org/10.1016/j.epsl.2010.08.017.

Xie Y, Dang X, Zhou Y, Hou Z, Li X, Jiang H, Zhou D, Wang J, Hai C, Zhou R. 2020. Using sediment grain-size characteristics to assess effectiveness of mechanical sand barriers in reducing erosion. Scientific Reports. 10(1):14009. doi:https://doi.org/10.1038/s41598-020-71053-3. https://www.nature.com/articles/s41598-020-71053-3.

Ziegler M, Jilbert T, Lange GJ de, Lourens LJ, Reichart G-J. 2008. Bromine counts from XRF scanning as an estimate of the marine organic carbon content of sediment cores. Geochemistry, Geophysics, Geosystems. 9(5):n/a. https://www.academia.edu/3380440/Bromine_counts_from_XRF_scanning_as_an_estimate_of_the_marine_organic_carbon_content_of_sediment_cores.

APPENDICES

Appendix A: List of the components counted in the 125 μm and 250 μm fractions

Depth (cm BSF)	Sediments	Fraction	Quartz	Micas	Other terrigenous	Benthic Foraminifera	Planktonic Foraminifera	Aggregates	Other biogenic
60-61	Core	125 μm	11	7	0	0	62	9	11
60-61	Core	250 μm	10	4	0	3	55	24	4
102-103	Core	125 μm	9	12	11	6	44	9	9
102-103	Core	250 μm	5	2	13	4	55	9	12
117-118	Black	125 μm	3	6	22	3	45	9	12
117-118	Black	250 μm	8	2	14	11	52	8	5
139-140	Core	125 μm	10	20	9	7	45	2	7
139-140	Core	250 μm	4	4	16	3	60	6	7
193-194	Black	125 μm	6	2	24	16	42	4	6
193-194	Black	250 μm	5	0	20	8	46	7	14
218-219	Core	125 μm	7	8	6	19	44	6	10
218-219	Core	250 μm	3	3	7	6	66	4	11
248-249	Core	125 μm	12	6	5	11	57	3	6
248-249	Core	250 μm	8	3	5	6	56	10	12
304-305	Black	125 μm	2	3	45	15	24	3	8
304-305	Black	250 μm	9	7	16	9	47	1	11

Appendix B: List of the grains counted in the selected smear slides

Sample ID	Depth (cm BSF)	Sediments	Clay	Biotite	Chlorite	Quartz	Feldspar	Opaque grains	Heavy minerals	Nannofossils	Foraminifera	Sponge spicule	Glauconite	Pyrite	Fe oxides	Organic matter
SM3	23	Core	25	3	0	0	10	2	0	54	4	1	1	0	0	0
SM7	60.3	Core	21	1	0	10	6	5	0	53	2	0	0	0	0	2
SM8	78.1	Core	29	3	0	5	2	6	0	53	1	0	0	0	0	1
SM 9b	95	Black	31	5	0	8	3	0	0	0	3	0	4	17	7	22
SM10	102.8	Core	21	4	0	8	4	10	0	48	3	0	0	0	0	2
SM 10b	117	Black	13	5	0	9	3	0	0	0	14	0	3	17	12	24
SM12	-21.6	Core	15	4	0	8	6	5	0	60	0	0	0	1	0	1
SM14	137.1	Core	16	0	0	10	7	5	0	55	0	0	0	0	0	7
SM1	139.5	Core	26	3	0	21	1	7	0	28	7	0	0	4	0	3
SM3	154	Black	7	0	3	3	5	0	13	0	19	0	7	16	0	27
SM5	194	Black	7	3	0	4	0	0	5	26	3	0	0	24	3	25
SM8	206.5	Black	6	3	0	7	0	0	5	22	0	0	0	17	13	27
SM10	219	Core	31	7	0	14	1	0	0	31	3	0	0	5	0	8
SM12	228.5	Black	7	1	0	9	6	0	0	13	0	0	0	36	3	25
SM14	239.5	Core	29	3	0	12	3	3	0	36	1	0	0	0	0	13
SM1	242	Black	8	2	0	8	2	0	0	11	0	0	0	43	4	22
SM2	248	Core	26	5	0	10	3	3	0	44	2	0	0	0	0	7
SM3	278	Core	22	0	11	10	4	12	0	34	1	0	0	0	0	6
SM5	302	Core	31	9	0	12	1	3	0	37	0	0	0	0	0	7
SM6	304	Black	9	6	0	5	7	0	0	7	2	0	1	36	4	23

Appendix C: Geometric method of moments extracted from Blott & Pye (2001)

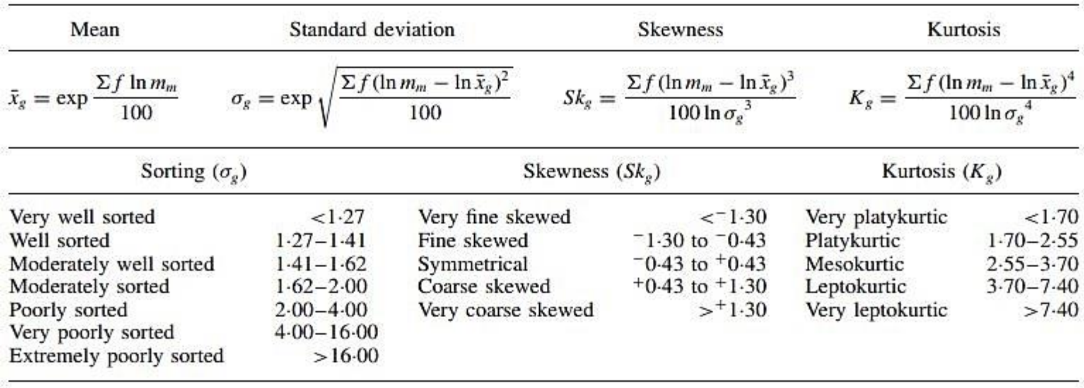

Mean	Standard deviation	Skewness	Kurtosis
$\bar{x}_g = \exp \frac{\Sigma f \ln m_m}{100}$	$\sigma_g = \exp \sqrt{\frac{\Sigma f (\ln m_m - \ln \bar{x}_g)^2}{100}}$	$Sk_g = \frac{\Sigma f (\ln m_m - \ln \bar{x}_g)^3}{100 \ln \sigma_g{}^3}$	$K_g = \frac{\Sigma f (\ln m_m - \ln \bar{x}_g)^4}{100 \ln \sigma_g{}^4}$

Sorting (σ_g)		Skewness (Sk_g)		Kurtosis (K_g)	
Very well sorted	<1·27	Very fine skewed	<$^{-}$1·30	Very platykurtic	<1·70
Well sorted	1·27–1·41	Fine skewed	$^{-}$1·30 to $^{-}$0·43	Platykurtic	1·70–2·55
Moderately well sorted	1·41–1·62	Symmetrical	$^{-}$0·43 to $^{+}$0·43	Mesokurtic	2·55–3·70
Moderately sorted	1·62–2·00	Coarse skewed	$^{+}$0·43 to $^{+}$1·30	Leptokurtic	3·70–7·40
Poorly sorted	2·00–4·00	Very coarse skewed	>$^{+}$1·30	Very leptokurtic	>7·40
Very poorly sorted	4·00–16·00				
Extremely poorly sorted	>16·00				

Appendix D: Bioturbation index (BI) card extracted from Gani (2020)

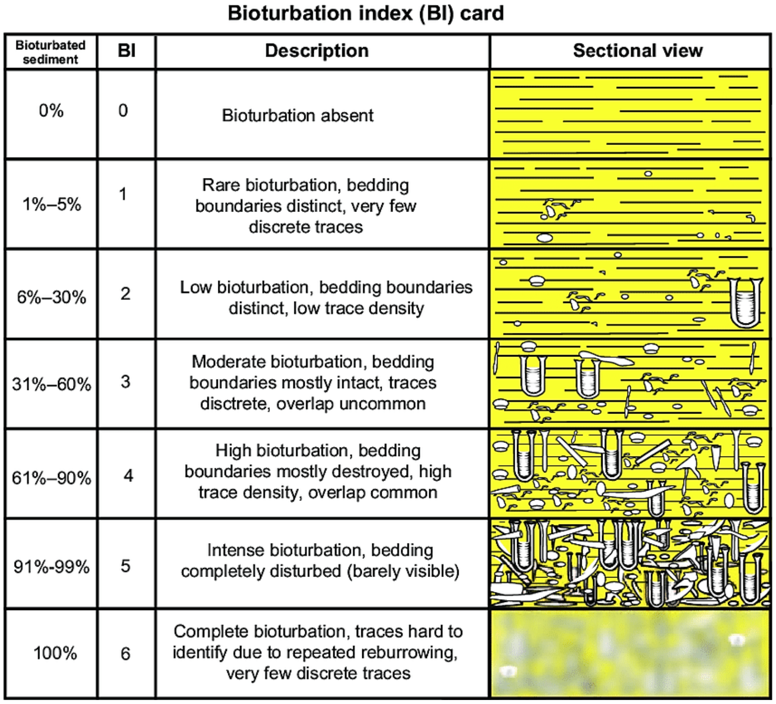

Bioturbation index (BI) card

Bioturbated sediment	BI	Description	Sectional view
0%	0	Bioturbation absent	
1%–5%	1	Rare bioturbation, bedding boundaries distinct, very few discrete traces	
6%–30%	2	Low bioturbation, bedding boundaries distinct, low trace density	
31%–60%	3	Moderate bioturbation, bedding boundaries mostly intact, traces disctrete, overlap uncommon	
61%–90%	4	High bioturbation, bedding boundaries mostly destroyed, high trace density, overlap common	
91%-99%	5	Intense bioturbation, bedding completely disturbed (barely visible)	
100%	6	Complete bioturbation, traces hard to identify due to repeated reburrowing, very few discrete traces	

Appendix E: Ichnological information modified from Dorador and Rodríguez-Tovar (2014)

Ichnotaxonomy	**Diagnostic morphological attributes**	**Ethology**
Taenidium	Tubular meniscate forms, simple, straight to sinuous, unlined with horizontal to oblique distribution. Length from 30 to 51 mm and diameter between 5–10 mm.	Feeding structure
Thalassinoides	Oval spots (6–11 mm wide) and horizontal to oblique smooth cylinders (22–43 mm long), corresponding to different sections of branching burrow systems.	Downwelling/feeding structure
Thalassinoides-like	Circular to subcircular cross-sections (6–12 mm wide) and cylindrical structures (15–20 mm long), with irregular wall and diffuse shape like *Thalassinoides*.	Downwelling/feeding structure
Zoophycos	Repeated spreiten structures, 4–11 mm wide, with sub-horizontal orientation. The structures show an alternation between dark and light lamellae material into the lamina. Correspond to cross sections of a helical coiled system of sub-horizontal lobes.	Feeding structure

Appendix F: Textural distribution (ternary diagram) – PC06

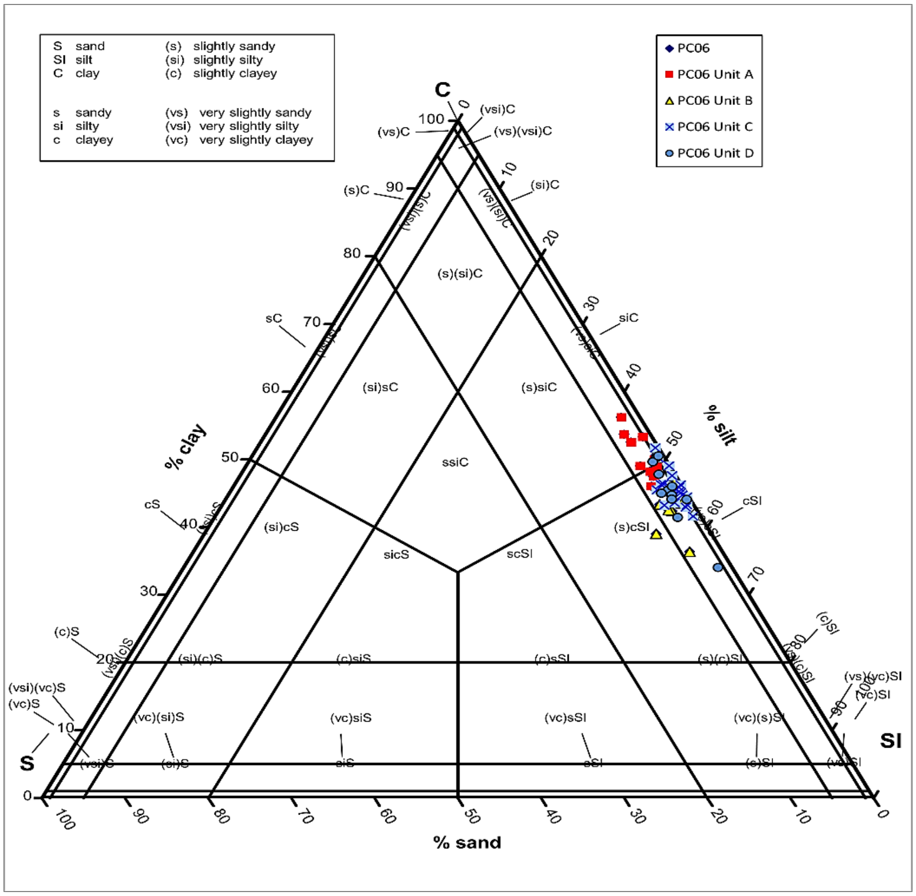

Appendix G: List of coccolithophorids species recognized in the smear slides

COCCOLITHOPHORIDS		**PERIOD**
Species	Photos (polarized light, 40x objective lens)	
Emiliania huxleyi (1)	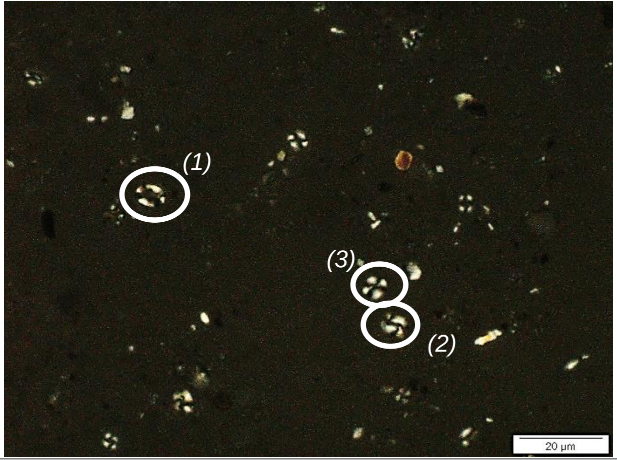	Pleistocene (1)
Reticulofenestra bisecta (2)		Late Oligocene (2)
Reticulofenestra haqii (3)		? (3)
Discoaster surculus (4)		Early Pliocene (4)
Discoaster hamatus (5)		Late Miocene (5)
Amaurolithus primus (6)	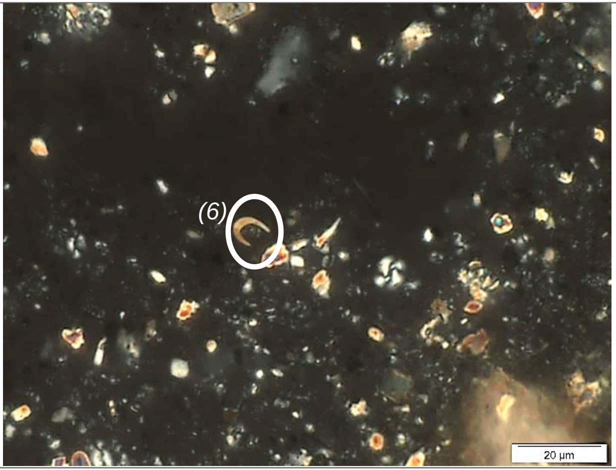	Early Pliocene (6)

Appendix H: R-script and results of the multivariate analysis (PCA)

```
library(Rcmdr)
library(FactoMineR)
library(ggplot2)
Dataset <- readXL("C:/Users/meime/TESE_2023/Data/PC06.xlsx", rownames=FALSE, header=TRUE, na="",
sheet="SAND(PCA)",
   stringsAsFactors=TRUE)
Dataset.PCA<-Dataset[, c("Benthic.Foram.", "Planktonic.Foram.", "Quartz", "Other.terrigenous", "Color",
  "Fraction")]
res<-PCA(Dataset.PCA , scale.unit=TRUE, ncp=5, quali.sup=c(5: 6), graph = FALSE)
res.hcpc<-HCPC(res ,nb.clust=-1,consol=FALSE,min=3,max=10,graph=TRUE)
print(plot.PCA(res, axes=c(1, 2), choix="ind", habillage=5, col.ind="black", col.ind.sup="blue",
  col.quali="#000080", label=c("ind", "ind.sup", "quali"),new.plot=TRUE, title="PCA Correlation - SAND
(PC06)"))
print(plot.PCA(res, axes=c(1, 2), choix="var", new.plot=TRUE, col.var="#000080", col.quanti.sup="blue",
  label=c("var", "quanti.sup"), lim.cos2.var=0, title="PCA Correlation - SAND (PC06)"))
summary(res, nb.dec = 3, nbelements=10, nbind = 10, ncp = 3, file="")
```

```
Call:
"res<-PCA(Dataset.PCA , scale.unit=TRUE, ncp=5, quali.sup=c(5: 6), graph = FALSE)"

Eigenvalues
                       Dim.1   Dim.2   Dim.3   Dim.4
Variance               2.494   0.999   0.417   0.089
% of var.             62.349  24.986  10.430   2.235
Cumulative % of var.  62.349  87.335  97.765 100.000

Individuals (the 10 first)
                Dist    Dim.1    ctr   cos2    Dim.2    ctr   cos2    Dim.3    ctr   cos2  
1           |  2.684 | -2.603 16.982  0.941 | -0.109  0.075  0.002 | -0.625  5.856  0.054 |
2           |  1.926 | -1.825  8.345  0.897 |  0.225  0.318  0.014 | -0.478  3.417  0.061 |
3           |  1.005 | -0.216  0.117  0.046 |  0.450  1.264  0.200 | -0.825 10.187  0.673 |
4           |  1.139 | -0.348  0.304  0.094 | -1.080  7.288  0.899 |  0.083  0.103  0.005 |
5           |  1.901 |  0.906  2.057  0.227 | -1.560 15.225  0.674 | -0.520  4.044  0.075 |
6           |  0.717 |  0.036  0.003  0.003 |  0.531  1.766  0.550 |  0.334  1.673  0.217 |
7           |  1.206 | -0.438  0.480  0.132 |  0.815  4.153  0.456 | -0.743  8.266  0.379 |
8           |  1.743 | -0.413  0.427  0.056 | -1.639 16.801  0.885 |  0.308  1.424  0.031 |
9           |  2.058 |  1.832  8.413  0.793 |  0.758  3.594  0.136 |  0.474  3.371  0.053 |
10          |  0.998 |  0.872  1.907  0.764 | -0.478  1.428  0.229 | -0.077  0.089  0.006 |

Variables
                     Dim.1    ctr   cos2    Dim.2    ctr   cos2    Dim.3    ctr   cos2  
Benthic.Foram.    |  0.658 17.340  0.432 |  0.622 38.738  0.387 |  0.424 43.053  0.180 |
Planktonic.Foram. | -0.877 30.868  0.770 | -0.282  7.984  0.080 |  0.349 29.192  0.122 |
```

```
Quartz            | -0.647 16.769  0.418 |  0.695 48.347  0.483 | -0.293 20.561  0.086 |
Other.terrigenous |  0.935 35.022  0.873 | -0.222  4.932  0.049 | -0.173  7.194  0.030 |

Supplementary categories
                    Dist    Dim.1   cos2  v.test    Dim.2   cos2  v.test    Dim.3   cos2  v.test
Black            |  1.387 |  1.375  0.983  2.612 | -0.054  0.002 -0.163 | -0.126  0.008 -0.584 |
Background       |  0.832 | -0.825  0.983 -2.612 |  0.033  0.002  0.163 |  0.075  0.008  0.584 |
125  µm          |  0.627 |  0.438  0.489  1.074 |  0.415  0.438  1.606 | -0.164  0.068 -0.982 |
250  µm          |  0.627 | -0.438  0.489 -1.074 | -0.415  0.438 -1.606 |  0.164  0.068  0.982 |

> remove(Dataset.PCA)
```

Appendix I: R-script and results of the clustering analysis (k-mean)

```
library(Rcmdr)
Dataset <- readXL("C:/Users/meime/TESA_2023/PC06.xlsx", rownames=FALSE, header=TRUE, na="",
  sheet="SMEAR SLIDES(kmean)", stringsAsFactors=TRUE)
df <- scale(Dataset)
kmeans (df, 2, iter.max=10, nstart=1)
K-means clustering with 2 clusters of sizes 12, 8

Cluster means:
        clay nannofossils organic.matter     pyrite
1  0.5695581    0.6846985     -0.7574365 -0.7002313
2 -0.8543371   -1.0270478      1.1361548  1.0503469

Clustering vector:
 [1] 1 1 1 2 1 2 1 1 1 2 2 2 1 2 1 2 1 1 1 2

Within cluster sum of squares by cluster:
[1]  8.545461 11.737267
 (between_SS / total_SS =  73.3 %)

Available components:

[1] "cluster"      "centers"      "totss"        "withinss"     "tot.withinss" "betweenss"    "size"
[8] "iter"         "ifault"

library(ggplot2, pos=16)
library(factoextra, pos=16)
```

```
.cluster <-  KMeans(model.matrix(~-1 + clay + nannofossils + organic.matter + pyrite, Dataset), centers = 2,
  iter.max = 10, num.seeds = 10)

.cluster$size # Cluster Sizes
[1] 12  8
.cluster$centers # Cluster Centroids
new.x.clay new.x.nannofossils new.x.organic.matter new.x.pyrite
1   24.33333          44.41667               4.750    0.8333333
2   11.00000           9.87500              24.375   25.7500000

.cluster$withinss # Within Cluster Sum of Squares
[1] 1811.50 2072.25

.cluster$tot.withinss # Total Within Sum of Squares
[1] 3883.75

.cluster$betweenss # Between Cluster Sum of Squares
[1] 11409.05

biplot(princomp(model.matrix(~-1 + clay + nannofossils + organic.matter + pyrite, Dataset)), xlabs =
  as.character(.cluster$cluster))

remove(.cluster)
```